

# JGR Solid Earth

## RESEARCH ARTICLE

10.1029/2023JB028571

### Key Points:

- A suite of faulted viscous shell models testing key parameters explain new observations from geodesy for the India-Asia collision
- The India-Asia collision is explained by the balance between buoyancy and boundary forces, slip on faults, and internal strength variations
- Central Tibetan Plateau has a vertically-averaged effective viscosity of  $\sim 10^{21}$  Pa s, 1–2 orders lower than the surrounding area

### Supporting Information:

Supporting Information may be found in the online version of this article.

### Correspondence to:

J. Fang,  
[eejf@leeds.ac.uk](mailto:eejf@leeds.ac.uk)

### Citation:

Fang, J., Houseman, G. A., Wright, T. J., Evans, L. A., Craig, T. J., Elliott, J. R., & Hooper, A. (2024). The dynamics of the India-Eurasia collision: Faulted viscous continuum models constrained by high-resolution Sentinel-1 InSAR and GNSS velocities. *Journal of Geophysical Research: Solid Earth*, 129, e2023JB028571. <https://doi.org/10.1029/2023JB028571>

Received 18 DEC 2023

Accepted 16 JUN 2024

### Author Contributions:

**Conceptualization:** Jin Fang, Gregory A. Houseman, Tim J. Wright

**Data curation:** Tim J. Wright

**Formal analysis:** Jin Fang, Gregory A. Houseman, Tim J. Wright, Tim J. Craig,

John R. Elliott, Andy Hooper

**Funding acquisition:** Jin Fang, Tim J. Wright

**Investigation:** Jin Fang

**Methodology:** Jin Fang, Gregory A. Houseman, Tim J. Wright, Lynn A. Evans

**Software:** Gregory A. Houseman, Lynn A. Evans

**Visualization:** Jin Fang, Gregory A. Houseman, Tim J. Wright, Lynn A. Evans

**Writing—original draft:** Jin Fang, Gregory A. Houseman, Tim J. Wright, Lynn A. Evans

**Writing—review and editing:** Jin Fang, Gregory A. Houseman, Tim J. Wright, Lynn A. Evans

**Supervision:** Gregory A. Houseman, Lynn A. Evans

**Project administration:** Jin Fang, Gregory A. Houseman, Tim J. Wright, Lynn A. Evans

**Resources:** Jin Fang, Gregory A. Houseman, Tim J. Wright, Lynn A. Evans

**Validation:** Jin Fang, Gregory A. Houseman, Tim J. Wright, Lynn A. Evans

**Formal analysis:** Jin Fang, Gregory A. Houseman, Tim J. Wright, Lynn A. Evans

**Methodology:** Jin Fang, Gregory A. Houseman, Tim J. Wright, Lynn A. Evans

**Software:** Gregory A. Houseman, Lynn A. Evans

**Visualization:** Jin Fang, Gregory A. Houseman, Tim J. Wright, Lynn A. Evans

**Writing—original draft:** Jin Fang, Gregory A. Houseman, Tim J. Wright, Lynn A. Evans

**Writing—review and editing:** Jin Fang, Gregory A. Houseman, Tim J. Wright, Lynn A. Evans

**Supervision:** Gregory A. Houseman, Lynn A. Evans

**Resources:** Jin Fang, Gregory A. Houseman, Tim J. Wright, Lynn A. Evans

**Validation:** Jin Fang, Gregory A. Houseman, Tim J. Wright, Lynn A. Evans

**Formal analysis:** Jin Fang, Gregory A. Houseman, Tim J. Wright, Lynn A. Evans

**Methodology:** Jin Fang, Gregory A. Houseman, Tim J. Wright, Lynn A. Evans

# The Dynamics of the India-Eurasia Collision: Faulted Viscous Continuum Models Constrained by High-Resolution Sentinel-1 InSAR and GNSS Velocities

Jin Fang<sup>1</sup> , Gregory A. Houseman<sup>1,2</sup> , Tim J. Wright<sup>1</sup> , Lynn A. Evans<sup>3</sup> , Tim J. Craig<sup>1</sup> , John R. Elliott<sup>1</sup> , and Andy Hooper<sup>1</sup> 

<sup>1</sup>COMET, School of Earth and Environment, University of Leeds, Leeds, UK, <sup>2</sup>Now at School of Geophysics and Information Technology, China University of Geosciences, Beijing, China, <sup>3</sup>School of Earth, Atmosphere and Environment, Monash University, Clayton, VIC, Australia

**Abstract** The distribution and magnitude of forces driving lithospheric deformation in the India-Eurasia collision zone have been debated over many decades. Here we test a two-dimensional (2-D) Thin Viscous Shell approach that has been adapted to explicitly account for displacement on major faults and investigate the impact of lateral variations in depth-averaged lithospheric strength. We present a suite of dynamic models to explain the key features from new high-resolution Sentinel-1 Interferometric Synthetic Aperture Radar as well as Global Navigation Satellite System velocities. Comparisons between calculated and geodetically observed velocity and strain rate fields indicate: (a) internal buoyancy forces from Gravitational Potential Energy acting on a relatively weak region of highest topography ( $>2,000$  m) contribute to dilatation of the high plateau and contraction on the margins; (b) a weak central Tibetan Plateau ( $\sim 10^{21}$  Pa s compared to far-field depth-averaged effective viscosity of at least  $10^{22}$ – $10^{23}$  Pa s) is required to explain the observed long-wavelength eastward velocity variation; (c) localized displacement on fault systems enables strain concentration and clockwise rotation around the Eastern Himalayan Syntaxis. We discuss the tectonic implications for rheology of the lithosphere, distribution of geodetic strain, and partitioning of active faulting and seismicity.

**Plain Language Summary** The collision of the Indian Plate with Eurasia has created the Tibetan Plateau, one of the largest deforming regions in the continents. The mode of deformation has been a focus for heated debate and has inspired two contrasting tectonic models: (a) The deformation is localized on major faults separating “blocks” or (b) the strain is distributed throughout a “continuum.” We approximate the India-Eurasia collision by treating the continent as a thin viscous shell with regional variations in strength, explicitly accounting for displacements on selected major faults. We present a suite of models to explain the key features of new geodetic measurements from satellites. The best-fit model involves a weak Tibetan Plateau, a particularly weaker central plateau, and four strong regions outside the plateau, and allows displacements on major faults. This represents the deformation field of the India-Eurasia collision zone as a combination of continuous distributed deformation and focused strain on major faults.

## 1. Introduction

The Tibetan Plateau was created by the collision of the Indian Plate with Eurasia and has long been a testing ground for models of continental deformation. It extends more than 2,000 km north of the Himalayan Frontal Thrust, where large active faults appear to have developed since middle Miocene (Duvall et al., 2013; Gan et al., 2021). Geodetic observations from Global Navigation Satellite System (GNSS) and Interferometric Synthetic Aperture Radar (InSAR) reveal a complex pattern of current deformation in the India-Eurasia collision zone (Figure 1). The Tibetan Plateau and its margins accommodate India's indentation into Eurasia by crustal shortening, widespread active faulting, folding and uplifting (Q. Wang et al., 2001). In the Eurasia fixed reference frame, the westward motion in the western Tibetan Plateau is tapered to zero while the eastward velocities increase over  $\sim 1,000$  km distance across the eastern plateau before decreasing rapidly outside the plateau (M. Wang & Shen, 2020). Deformation within the plateau and the Tian Shan to the north is broadly distributed whereas outside these areas there are large undeforcing regions with deformation mainly affecting the perimeter of these regions (Ge et al., 2015; W. Li et al., 2022; M. Wang & Shen, 2020; Zheng et al., 2017). One of these undeforcing regions, the Tarim Basin between the plateau and Tian Shan, has been observed to rotate clockwise at a rate of

© 2024. The Author(s).

This is an open access article under the terms of the [Creative Commons Attribution License](https://creativecommons.org/licenses/by/4.0/), which permits use, distribution and reproduction in any medium, provided the original work is properly cited.

**Supervision:** Tim J. Wright, Tim J. Craig, John R. Elliott, Andy Hooper  
**Validation:** Jin Fang, Gregory A. Houseman  
**Visualization:** Jin Fang  
**Writing – original draft:** Jin Fang  
**Writing – review & editing:** Jin Fang, Gregory A. Houseman, Tim J. Wright, Lynn A. Evans, Tim J. Craig, John R. Elliott, Andy Hooper

~0.4–0.6°/Myr with respect to Eurasia since the Cenozoic era (Avouac & Tapponnier, 1993; Craig et al., 2012; Z.-K. Shen et al., 2001; M. Wang & Shen, 2020; J. Zhao et al., 2019).

While some major strike-slip faults in the Tibetan Plateau show strain concentrations (Ge et al., 2015; Kreemer et al., 2014), there are also areas of diffuse strain (Zheng et al., 2017). The high plateau is dilating at a rate of ~10–20 nanostrain/yr (Ge et al., 2015; Molnar & Deng, 1984; Wright et al., 2023; Zheng et al., 2017). E-W extension occurs throughout the plateau interior through a set of north-south striking rifts/grabens and conjugate strike-slip faulting (Molnar & Tapponnier, 1978; H. Wang et al., 2019); the northern and southern regions of the Tibetan Plateau show similar rates of dilatation in short-term geodetic data (Ge et al., 2015), although geological data suggest arc-parallel extension rates in the plateau may be higher nearer the Himalayan arc (Copley et al., 2011). The northeastern Tibetan Plateau and the eastern and southern margins of the plateau, as well as the Tian Shan region, are experiencing rapid contraction (England & Molnar, 2015; J. Li et al., 2022; Y. Li et al., 2018; Metzger et al., 2020, 2021; Molnar & Tapponnier, 1978; Ou et al., 2022; Q. Wang et al., 2001; Zhu et al., 2022). The southeastern Tibetan Plateau rotates clockwise around the eastern Himalayan syntaxis (EHS) (Gan et al., 2021; Y. Li et al., 2019; Z. Shen et al., 2005; M. Wang & Shen, 2020; Q. Wang et al., 2001; W. Wang et al., 2017, 2021; Zheng et al., 2017).

How best to understand the deformation field produced by the India-Asia collision has been a subject of extensive debate (Bendick & Flesch, 2013; Dal Zilio et al., 2021; Searle et al., 2011; Thatcher, 2009; H. Zhang et al., 2020; P. Zhang, 2013). Since the early days of plate tectonics, which beautifully explains the motion of oceanic plates, it has been recognized that deformation of the continents cannot be described by the motion of only a few large plates, with seismicity focused around their edges (McKenzie, 1972). Nevertheless, a popular approach for characterizing continental deformation is to model the deformation as rotation and translation of a number of blocks, or microplates, each following the kinematic rules of plate tectonics (Avouac & Tapponnier, 1993; Y. Li et al., 2018; McCaffrey et al., 2000; McClusky et al., 2001; Meade & Hager, 2005; Socquet et al., 2006; Thatcher, 2007; Wallace et al., 2004, 2005; W. Wang et al., 2017, 2021). In most block models, strain concentrations only occur along the block boundaries, although a few allow for strain within block interiors (Q. Chen et al., 2004; Loveless & Meade, 2011). Avouac and Tapponnier (1993) proposed the first 4-microplate model for the India-Asia collision based primarily on geological observations. Q. Chen et al. (2004) constructed a deformable block model to explain GNSS observations from 45 stations. The trend in subsequent models has been to increase the number of blocks to fit more GNSS observations as they become available (Y. Li et al., 2018; Loveless & Meade, 2011; Styron, 2022; Thatcher, 2007; W. Wang et al., 2017, 2021). These block models are helpful for deriving slip rates and locking depths for major faults and are widely used in seismic hazard analysis (Y. Li et al., 2018; Styron, 2022; W. Wang et al., 2017, 2021). They can naturally describe large undefining areas and focused strain around faults. If enough blocks are used, these models can reproduce the observed displacement rate field to the desired accuracy. However, because the models are purely kinematic, they have no predictive power and cannot be used to test the underlying causes of the observed deformation or to understand the balance of forces acting on blocks. The geodetic strain can be described in the short term, even with an elastic model, but appealing to elastic strain as an explanation of strain rates sustained on geological time-scales is not logically self-consistent. In addition, as focused strain might not coincide with mapped faults (H. Wang & Wright, 2012; H. Wang et al., 2019), a simple block model could underestimate the likelihood of earthquakes occurring on unknown faults due to our imperfect knowledge of the boundaries of crustal blocks, which must be defined a priori; all earthquakes by definition must occur on block boundaries in such a framework.

An alternative approach has been to treat continents as a continuum, with deformation modeled as a viscous fluid acting under the influence of the internal and boundary forces applied, and a simply parameterized viscous constitutive law (England & McKenzie, 1982; Flesch et al., 2001). In these models, deformation is distributed throughout the layer representing the lithosphere. England and McKenzie (1982) simplified the deformation to a two-dimensional (2-D) problem by treating the lithosphere as a thin viscous sheet originally developed for a flat layer with vertically-averaged properties. England and Houseman (1986) applied the viscous sheet formulation assuming a uniform viscosity coefficient to analyze the dynamics of the India-Eurasia collision. In such models, strain is focused where gradients of Gravitational Potential Energy (GPE) are greatest, and on parts of the boundary where the boundary forces change rapidly. With more and more observations and stronger computational power, more complexity in models has been required to explain the observations (Bischoff & Flesch, 2018, 2019; Flesch et al., 2001; Lechmann et al., 2014; Neil & Houseman, 1997; Vergnolle et al., 2007). Early viscous continuum models did not predict the strain concentrations observed in dense geodetic data around major faults. However, Dayem, Houseman, and Molnar (2009) and Molnar and Dayem (2010) showed that viscous continuum

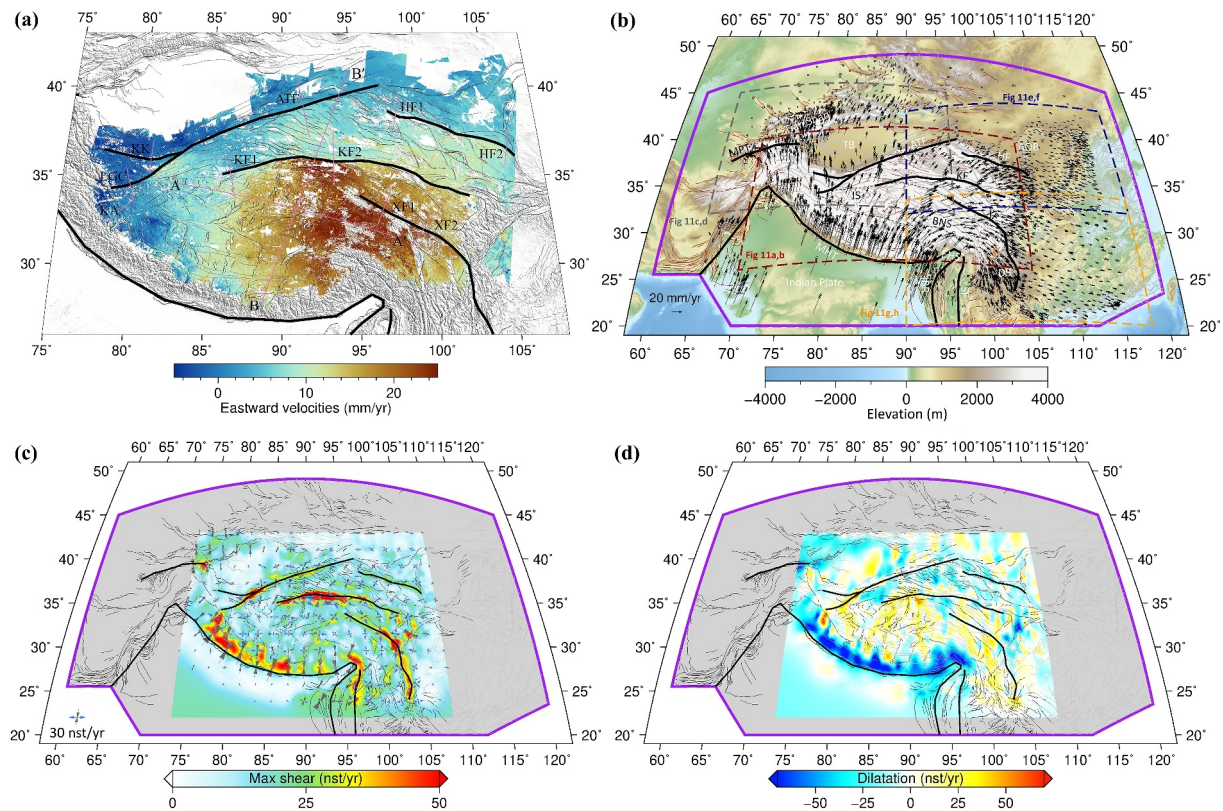


**Figure 1.** (a) Eastward velocity map constructed from ascending and descending Sentinel-1 Interferometric Synthetic Aperture Radar line-of-sight velocities (Wright et al., 2023). Pink lines show the location of profiles presented in Figure 7. Thin black lines are fault traces from the Global Earthquake Model Global Active Faults Database (Styron & Pagani, 2020). Gray lines depict fault traces from China Active Fault Database (Xu, 2022). Thick black lines are model faults incorporated in numerical simulations in this study. (b) Global Navigation Satellite System velocities compiled from published studies (see Text S1 in Supporting Information S1 for more details). Purple polygon shows the boundary of the calculation domain. Dashed lines show the extents of zoomed views shown in Figure 11. Abbreviations in (a) and (b): AOB, Alxa-Ordos Basin; ATF, Altyn Tagh Fault; BNS, Bangong-Nujiang Suture; DB, Dianzhong Block; EHS, Eastern Himalayan Syntaxis; HF, Haiyuan Fault; IBR, Indo-Burma Ranges; JS, Jinsha Suture; KA, Karakoram Fault; KF, Kunlun Fault; KK, Karakash Fault; LGC, Longmu-Gozha Co Fault; LXF, Lijiang-Xiaojinhe Fault; MHT, Main Himalayan Thrust; MPT, Main Pamir Thrust; SB, Sichuan Basin; SF, Sagaing Fault; TB, Tarim Basin; XF, Xianshuihe-Xiaojiang Fault. (c and d) Maximum shear and dilatation strain rates from the geodetically-derived velocity field (Wright et al., 2023). The deformation is distributed throughout the India-Eurasia collision zone. Note that we observe shear strain concentrations on major faults (c), dilatation within the high plateau, and contraction (negative dilatation) along the plateau margins, as indicated by the yellowish and bluish colors, respectively, in (d). Arrow pairs in (c) show principal strain rates, with contraction shown in gray and extension shown in blue.

models can concentrate strain at regions of strength contrast. Lechmann et al. (2014) and Bischoff and Flesch (2018, 2019) achieved strain concentrations by explicitly allowing weaker regions to represent localized strain associated with major faults. Haines and Sutherland (2018) incorporated fault discontinuities into a thin viscous sheet model. They introduced an arbitrary weighting factor to balance constraints from geodetic data with the requirements of a self-consistent force balance, with the aim of achieving a better fit to observations. Nevertheless, it is worth noting that this adjustment may deviate from physical dynamic principles (e.g., Hirschberg & Sutherland, 2022).

The strength of the lower crust exhibits considerable variability due to a combination of factors including compositions (felsic or mafic), water contents, and temperatures (Brace & Kohlstedt, 1980; Bürgmann & Dresen, 2008; Rybacki et al., 2006; Stenvall et al., 2019; Y. Wang et al., 2012). Some authors have argued that the lower crust is so weak that it is decoupled from both the upper crust and the upper mantle. W. Zhao and Morgan (1987) presented a model in which the stronger Indian crust injects into the weaker fluid-like lower crust of the Tibetan Plateau. Based on geologic and GNSS observations, Royden et al. (1997, 2008) presented a lower crustal flow model in the eastern Tibetan Plateau where crustal material flows around the EHS and also around the strong Sichuan Basin. They argued that the lower crust escapes from beneath the central plateau through regions where crust is weak (Clark & Royden, 2000), and that the morphology of the eastern plateau reflects crustal

material flows. Copley and McKenzie (2007) interpreted the formation of the geometry of the EHS by gravitationally driven fluid flow in both the southern Tibetan Plateau and the Indo-Burman Ranges. Bischoff and Flesch (2019) approximated the three-dimensional (3-D) India-Eurasia deformation with creeping flow, with a weak lower crust required to explain the observed vertical surface velocities. Contrary to such models, however, a strong coupling between the crust and the mantle is inferred (Holt, 2000; McNamara et al., 1994; Silver, 1996; Sol et al., 2007). Rey et al. (2010) show that large-scale (>150 km) relative displacement of the lower and upper crust is unlikely and the rate of lower crustal flow is an order of magnitude smaller than previously suggested for the eastern Tibetan Plateau (i.e., 1 cm/yr instead of 10 cm/yr). Their results justify a key assumption of the Thin Viscous Shell (TVS) method that the lithosphere deforms coherently with depth, that is, horizontal velocity is independent of depth and horizontal tractions can be vertically averaged.

Lower crustal channel flow has also been invoked for models in which material in a partially molten mid-crust is extruded southward from beneath the southern Tibetan Plateau toward the high Himalayan front (Godin et al., 2006; Grujic et al., 2002; Law et al., 2004; Searle & Szulc, 2005; Searle et al., 2003, 2006, 2011). Assuming high erosion rates on the Himalayan front, Beaumont et al. (2001) interpret the Himalayan tectonics by a low-viscosity channel flow and ductile extrusion, which causes high-grade metamorphic rocks to be exhumed. However, Copley et al. (2011) argue that the mechanical coupling between the upper crust of the southern Tibetan Plateau and the underthrust Indian crust is inconsistent with the low-viscosity “channel flow” models in the southern plateau. Flesch et al. (2018) suggest surface GNSS velocities contain little or no information about 3-D dynamics. Penney and Copley (2021) further suggest that the temporal evolution of topography in the southeastern Tibetan Plateau can be explained without invoking a low-viscosity lower crustal channel. Nie et al. (2023) argue that the melt volume percentage is too low to induce crustal channel flow in the central plateau.

Both block models and continuum models are over-simplifications of a more complex reality that requires both distributed deformation and, at least in the near surface, slip on faults (Houseman et al., 2023; Thatcher, 2009). Ductile deformation is manifested in almost any geological environment where the temperatures are sufficiently great, but near surface deformation typically occurs by faulting. In the case of large-scale continental faults, seismic activity is typically restricted to the upper 15 km or so (Wright et al., 2013), but there is increasing evidence that localized deformation is moderated by ductile shear zones that can extend through the crustal layer and possibly into the mantle (Alvizuri & Hetényi, 2019; Bürgmann & Dresen, 2008; Kelemen & Dick, 1995; Leloup et al., 1999; Scholz & Choi, 2022; Thybo et al., 2000; Vauchez et al., 2012; Warner, 1990). Hence the deformation field in general can be represented as a continuum modulated by major faults. Continuum models are appealing in that they have the potential to explain large-scale deformation with relatively few adjustable parameters. Garthwaite and Houseman (2011) demonstrate the validity of the 2-D thin viscous sheet approximation for continental collision provided that the indenter width is larger than the thickness of the lithosphere. In this study, we employ the adapted 2-D TVS continuum model of England et al. (2016), explicitly modified to account for displacement discontinuities on faults. Although a linear constitutive relation between stress and strain rate is often adopted in 3-D numerical modeling (Bischoff & Flesch, 2019; Copley & McKenzie, 2007; Lechmann et al., 2014; M. Liu & Yang, 2003; Penney & Copley, 2021; Royden et al., 1997; F. Shen et al., 2001), we assume a non-Newtonian (power law) viscous rheology. Early geodynamic simulations have primarily relied on information from topography, Quaternary fault slip rates, and seismic moment tensors (England & Houseman, 1986; England & Molnar, 2005; Flesch et al., 2001). The constantly improving accuracy and resolution of the geodetic observations now allow us to use geodetic data as a primary constraint on geodynamic models of the present-day deformation field. We present a suite of faulted viscous continuum models constrained by new geodetic observations of the India-Eurasia collision (Wright et al., 2023). This allows us to explore (a) the importance of internal buoyancy forces from GPE, (b) the relationship between slip resistance on faults and associated ductile deformation, and (c) the role of rheological/strength contrasts and how they modulate and localize deformation.

## 2. Data and Methods

### 2.1. Data

We use constraints from new high-resolution InSAR (Figure 1a, Wright et al., 2023) and published GNSS horizontal velocity fields (Figure 1b) to test the faulted viscous continuum model. The GNSS data are compiled from previously published studies (see Text S1 in Supporting Information S1 for more details about the compilation, Ashurkov et al., 2018; Aung et al., 2016; Barman et al., 2016; Bisht et al., 2021; Crupa et al., 2017;

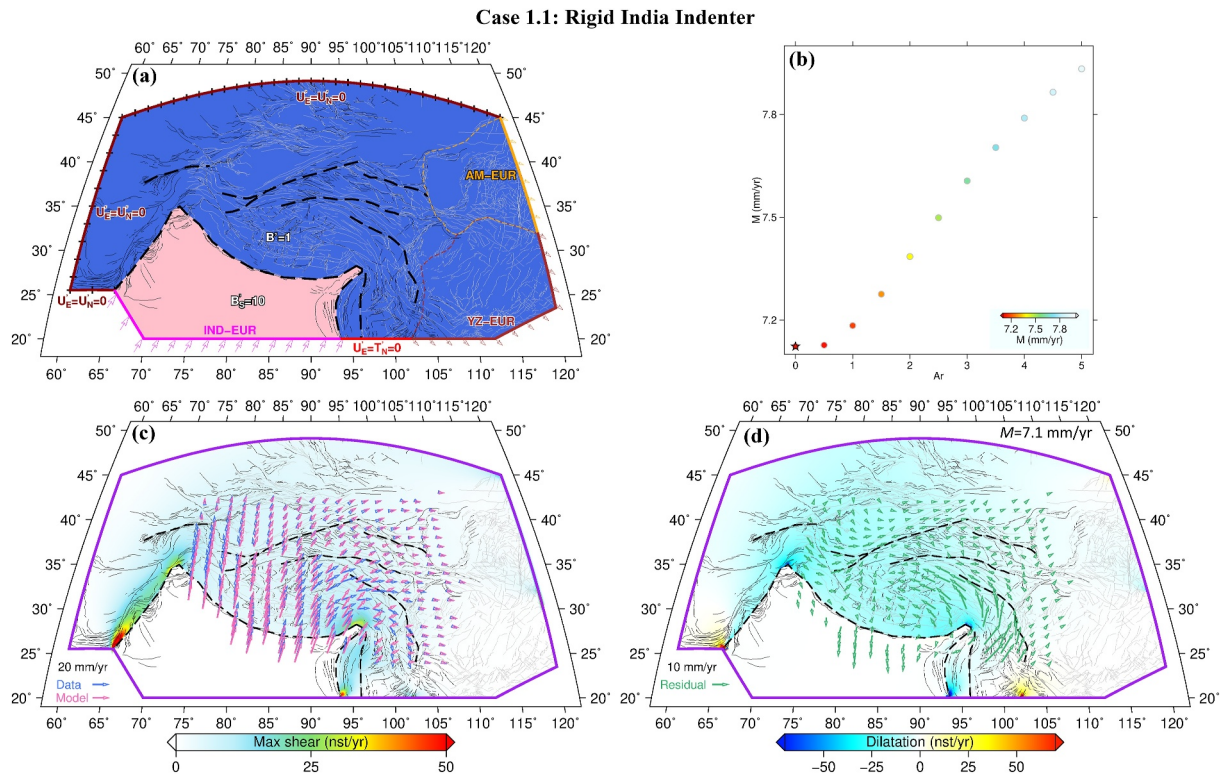


**Figure 2.** (a) Schematic diagram illustrating boundary conditions and model rheological coefficients for Case 1.1: rigid India indenter. Thin black and gray lines are fault traces from the Global Earthquake Model Global Active Faults Database (Styron & Pagani, 2020) and China Active Fault Database (Xu, 2022), respectively. Model faults are shown in dashed lines, meaning they are “locked” (no-slip) in this case. Boundaries of the Amur and Yangtze plates are depicted as dashed orange and brown lines, respectively. (b) Root mean square misfit,  $M$ , as a function of the Argand number. The minimum misfit is marked as a star. (c) Model fits (pink arrows) to the sampled observations (blue arrows) derived from joint inversion of Interferometric Synthetic Aperture Radar and Global Navigation Satellite System. The underlying map shows the maximum shear strain rate field from model velocities for this case. (d) Residual vectors (calculated-observed velocities), underlain by model dilatation strain rate field. In the strain-rate scales,  $nst = 10^{-9}$ .

Devachandra et al., 2014; Diao et al., 2019; Dumka et al., 2014, 2018; Fazilova et al., 2018; Frohling & Szeliga, 2016; Gahalaut et al., 2018, 2019; Gautam et al., 2017; Ge et al., 2015; Guo et al., 2018; Gupta et al., 2015; Jade et al., 2011, 2014, 2017, 2020; Jouanne et al., 2014; Kreemer et al., 2014; Kundu et al., 2014; Y. Li et al., 2017; Mallick et al., 2019; Marechal et al., 2016; Metzger et al., 2020; Y. Pan & Shen, 2017; Y. Pan et al., 2018, 2019; Z. Pan et al., 2020; Perry et al., 2019; Rui & Stamps, 2019; Sharma et al., 2020; Steckler et al., 2016; Su et al., 2018; D. Wang et al., 2020; M. Wang & Shen, 2020; W. Wang et al., 2017; Vernant et al., 2014; Yadav et al., 2019, 2021; B. Zhao et al., 2015, 2017; Zheng et al., 2017; Zhou et al., 2016; Zubovich et al., 2016). Both GNSS and InSAR data sets are fixed to a Eurasia reference frame. The combined geodetic velocities at observation points in the InSAR and GNSS are interpolated from the velocities at each node of the triangular mesh derived from the *velmap* approach (H. Wang & Wright, 2012). This combined geodetic solution fits the GNSS measurements with a root mean square (RMS) residual of 1.2 mm/yr and matches the InSAR measurements with an RMS of 1.7 mm/yr (Wright et al., 2023).

For the purpose of computational efficiency, we obtain a relatively sparse set of velocity vectors by a weighted average of the combined geodetic observations (Wright et al., 2023). We sub-sample the observed geodetic velocity field onto a  $2^\circ$  (longitude) by  $1^\circ$  (latitude) grid using a Gaussian weight (half-width at half-height of the weight function of  $0.593^\circ$ ) of all samples within  $0.5^\circ$  distance, and exclude measurements within a 10 km radius of model faults, to produce a total of 262 points used to constrain the TVS models (blue arrows in Figure 2c). This is efficient and effective to constrain the geodynamic models aiming to match the key features of the broad-scale, systematic patterns of the velocity field. We further evaluate our models by examining velocity profiles in the interior of the plateau at high resolution (Figure 1a). We also test our models using a more extensive set of horizontal GNSS measurements compiled from published literature (Figure 1b and Text S1 in Supporting

**Table 1**

Summary of Model Cases and Fit to Key Observable Features of the Geodetically-Derived Velocity Field in the India-Asia Convergence Zone

Key observations	Case 1: Lateral heterogeneity in viscosity coefficient				Case 2: Allowing displacements on selected major faults		
	Case 1.1: Rigid India indenter	Case 1.2: Embedding strong Indian plate, Tarim, Sichuan, and Alxa-Ordos basins	Case 1.3: Weak area of high topography	Case 1.4: Further weakened central Tibetan Plateau	Case 2.1: Absence of weak zone	Case 2.2: Embedding weak region of high topography	Case 2.3: Further weakened central Tibetan Plateau
Distributed deformation throughout the India-Eurasia collision zone	✓	✓	✓	✓	✓	✓	✓
Dilatation of high plateau	×	×	✓	✓	×	✓	✓
Contraction on the margins of plateau	Partly	Partly	✓	✓	Partly	✓	✓
Smooth, long-wavelength eastward velocity variation away from major faults	×	×	×	✓	×	×	✓
Strain concentrations on major faults	×	×	Partly	Partly	✓	✓	✓
Asymmetric eastward velocity gradient across the Tibetan Plateau	×	×	Partly	Partly	✓	✓	✓
Clockwise rotation around the EHS	×	×	×	×	×	✓	✓
Clockwise rotation of the Tarim basin (rotation rate, °/Myr) <sup>a</sup>	−0.158	−0.165	−0.290	−0.323	−0.378	−0.505	−0.549
Best-fit Argand number	0	0.5	3.5	4	1	3	3
RMS misfit (mm/yr) <sup>b</sup>	7.1	6.9	5.7	5.1	4.8	3.7	3.4

<sup>a</sup>The rotation rate is calculated based on model GNSS velocities within the Tarim block for each case, anti-clockwise positive. The rotation rate of the Tarim basin derived from GNSS observations (Figure 1b) is  $-0.592^\circ/\text{Myr}$ . <sup>b</sup>RMS misfit to horizontal velocities from joint inversion of InSAR and GNSS.

Information S1). Excluding GNSS measurement points that are too close to model faults (<10 km) or too close together (<10 km) and have greater uncertainty, we use 2,783 GNSS measurements as constraints on the velocity field computed from the faulted continuum dynamic model. Since the observation points are defined as nodes in the finite element mesh for numerical calculations, nodes that are too close together or too close to model faults can result in triangles that are too small or too distorted, and may produce computational error. As our 2-D model does not represent the concept of a locked thin elastic lid overlying a ductile shear zone, we simulate the effect of the thin elastic lid by applying Gaussian filtering to the model velocity field before calculating the strain rate field. More importantly, the focused strain on the faults enables a more accurate representation of the broader-scale velocity distribution away from the faults.

Our dynamic models aim to match several key features revealed in the geodetic velocity and strain rate fields (Table 1, Figures 1, 2c, and 7).

1. The deformation is broadly distributed throughout the India-Eurasia collision zone (Figure 1).
2. The high plateau is dilating (Figure 1d).
3. The margins of the plateau show compressional strain (Figure 1d).
4. There is a smooth, long-wavelength eastward velocity variation away from major faults, with  $\sim 20$  mm/yr difference over  $\sim 1,400$  km distance (Figure 7a).
5. Apparent velocity contrasts observed across the major faults (Figures 1a and 7) represent strain concentrations on these structures (Figure 1c).

6. In the Eurasia-fixed reference frame, westward motion in the western plateau tapers to zero, while eastward velocities increase over  $\sim 1,000$  km in the eastern plateau before rapidly decreasing outside it (i.e., asymmetric eastward velocity gradient across the plateau, Figures 1b and 2c).
7. The southeastern plateau rotates clockwise around the EHS (Figures 1b and 2c).
8. The Tarim basin rotates clockwise at a rate of  $\sim 0.6^\circ/\text{Myr}$  (Figures 1b and 2c).

## 2.2. Methods

### 2.2.1. Power Law Rheology in a Faulted Ductile Medium

The vertically-averaged rheology of the TVS is described by a power law relation between deviatoric stress and strain rate (England & McKenzie, 1982; Sonder & England, 1986):

$$\bar{\tau}_{ij} = B\dot{E}^{\left(\frac{1}{n}-1\right)}\dot{\epsilon}_{ij} \quad (1)$$

where  $\bar{\tau}_{ij}$  is the  $ij$ th component of the deviatoric stress averaged over the thickness of the lithosphere,  $L$ ,  $\dot{\epsilon}_{ij}$  is the  $ij$ th component of the strain rate tensor (assumed constant with depth), and  $\dot{E}$  is the second invariant of the strain rate tensor:

$$\dot{E} = \sqrt{\dot{\epsilon}_{kl}\dot{\epsilon}_{kl}} \quad (2)$$

The fluid is assumed to be incompressible ( $\dot{\epsilon}_{kk} = 0$ ).

The viscosity coefficient,  $B$ , and the power law exponent,  $n$ , define the physical properties of the lithosphere. In this study, we use  $n = 3$ , which is suitable for a lithosphere where depth-averaged rheology is dominated by the power law creep of olivine (Brace & Kohlstedt, 1980; Karato et al., 1986; Kirby & Kronenberg, 1987), whereas large  $n$  represents plastic behavior (Dayem, Houseman, & Molnar, 2009; Dayem, Molnar, et al., 2009; Goetze et al., 1978; Schmalholz & Fletcher, 2011; Sonder & England, 1986). The effective viscosity is

$$\eta_{eff} = \frac{1}{2}B\dot{E}^{\left(\frac{1}{n}-1\right)} \quad (3)$$

Note that for non-Newtonian fluids ( $n \neq 1$ ) the effective viscosity is dependent on strain rate.

The GPE is calculated assuming local isostatic balance of topography ETOPO1 (Amante & Eakins, 2009) smoothed with a Gaussian filter sigma of 3 km. We define a reference strain rate as the ratio,  $\frac{U_0}{L}$ , of the scale velocity to the thickness of the lithosphere. The Argand number,  $Ar$ , as defined by England and McKenzie (1982), represents the relative importance of gravitational buoyancy related stress to viscous stress required to deform the lithosphere at the reference strain rate:

$$Ar = \frac{g\rho_c L \left(1 - \frac{\rho_c}{\rho_m}\right)}{B_0 \left(\frac{U_0}{L}\right)^{\frac{1}{n}}} \quad (4)$$

where  $g$  is the gravitational acceleration,  $\rho_c$  and  $\rho_m$  are the average densities of crust and mantle, respectively, and  $B_0$  is the scale factor for the viscosity coefficient.  $U_0$  is determined by minimizing the RMS misfit function:

$$M = \left[ \frac{1}{N} \sum_{i=1}^N |U_i - U_0 U_i'|^2 \right]^{\frac{1}{2}} \quad (5)$$

where  $U_i$  is the  $i$ th observed velocity, and  $U_i'$  is the dimensionless velocity of the same site in the calculation. In the dimensionless force balance, the Argand number multiplies the lateral gradient of GPE, scaling the force that pushes the layer away from regions of high GPE. As the Argand number increases, gravitational spreading of

regions with high GPE plays a more significant role and the lithosphere flows more in response to thickening (England & McKenzie, 1982).

We assume that the continuum deformation may be interrupted by slip on model fault structures, with resistance to displacement proportional to the slip rate in the horizontal plane. Therefore, we assume for the depth-averaged shear traction in tangential ( $\sigma_t$ ) and normal ( $\sigma_n$ ) directions:

$$\sigma_t = f_t \Delta U_t \quad (6)$$

$$\sigma_n = f_n \Delta U_n \quad (7)$$

where  $f_t$  and  $f_n$  represent the fault-resistance coefficients in tangential and normal directions, respectively, with zero implying a free-slipping fault and infinity meaning a “locked fault” where there is no focused slip on the structure (see Section 4.1 for more details). The depth-averaged shear traction for these model faults is assumed dominated by the behavior of ductile shear zones beneath the seismically active layer. In representing a dynamically consistent formulation that averages over earthquake cycle and depth, the fault resistance coefficient should not be confused with the concept of fault friction typically used in representing rate-and-state models of earthquake instability (e.g., Marone, 1998; Scholz, 1998).

We explicitly allow for displacement discontinuities across major faults (Altyn Tagh, Haiyuan, Kunlun, Xianshuihe-Xiaojiang, Sagaing, Main Pamir Thrust, Main Himalayan Thrust faults, and Indo-Burma Ranges) in the India-Asia collision zone. These are structures where InSAR and GNSS reveal apparent strain contrasts (Figure 1) that cannot easily be explained by a classic continuum model. While many more faults have been mapped, we only add faults to our continuum model where they are needed to match the observed velocities and strain rates. All model faults and internal structures incorporated in our numerical experiments are compatible with the first-order geological observations (Q. Deng et al., 2003; Jiao et al., 2023; Styron & Pagani, 2020; L. Wang & Barbot, 2023; Xu, 2022). Although many other faults are mapped and have a history of activity in the region, the present-day localized strain rate on many of the mapped faults is not evident in the geodetic velocity field.

### 2.2.2. Boundary Conditions and Internal Structures

We use the adapted finite element code *basil* (Houseman, 2023; Houseman et al., 2008) for instantaneous numerical modeling. The program solves the stress-balance equations using the finite element method described by Houseman and England (1986) amended to represent a deformation field on a spherical shell, as used by England et al. (2016). The triangular mesh is produced using the *Triangle* package (Shewchuk, 2002) and has been adapted by duplicating nodes along the faults to allow discontinuities in the calculated velocity field. The mesh includes nodes at all the observation points used to constrain the numerical simulations. The velocity field uses a quadratic interpolation on six node triangles. The elements are variable in shape and size and are subdivided until each area is smaller than 0.2 (dimensionless, Figure S1a in Supporting Information S1). All quantities in a calculation are dimensionless. The fault-resistance coefficient has a dimension of stress/velocity, depending on the choice of  $Ar$ . Its scale factor is

$$f_0 = \frac{B_0 \left(\frac{U_0}{R}\right)^{\frac{1}{n}}}{U_0} \quad (8)$$

where  $R$  is the radius of the Earth. Since we use a spherical shell, the natural length unit is the radian. Distances are therefore scaled by  $R$  in the dimensionless calculations. Further details on the dimensionalization of *basil* calculations can be found in Text S2 of Supporting Information S1.

Figure 2a shows the boundary conditions. In the *basil* software, the default boundary condition is traction-free relative to the lithostatic condition. We have imposed a series of velocity boundary conditions along segments, guided by available data on plate motions and geodetic observations. We set velocities to zero along the northern, western, and part of southern boundaries which are assumed fixed to the undeforming Eurasian plate ( $U'_E = U'_N = 0$ ). We set plate rotations on three boundary sections; we use the reconstructed motion of the Indian Plate relative to Eurasia (IND-EUR) from DeMets et al. (2020) and MORVEL velocities of Yangtze (YZ-EUR)

and Amur Plates (AM-EUR) from DeMets et al. (2010). They are compatible with our geodetic observations as they are all referenced to the Eurasia plate. We set the rotation rate of the Indian Plate to 1 (dimensionless) and scale those of Yangtze and Amur Plate boundary segments in proportion. The velocity scale  $U_0$  is determined from the solution by minimizing the misfit (Equation 5) between observed and dimensionless model velocities. The velocities on the part of the southern boundary that crosses Myanmar are poorly constrained and we set zero velocity in the east direction and zero traction (relative to lithostatic) in the north direction ( $U'_E = T'_N = 0$ , Figure 2a); this allows for north-south motion along that boundary segment, as implied by GNSS measurements in that region (Figure 1b).

The complexity of the observed deformation styles indicates the convergence of India with Eurasia is not the only factor influencing the distribution of displacements. The internal buoyancy forces from GPE and heterogeneities in lithospheric strength also contribute to the regional deformation pattern (England & Houseman, 1985; England & Molnar, 2005). Assuming that the background dimensionless depth-averaged viscosity coefficient ( $B'$ ) is 1, we also investigate the influence of regional variations in internal strength by embedding strong Indian Plate, Tarim, Sichuan, and Alxa-Ordos Basins ( $B'_S = 10$ ) (Figures 2a and 3a), weakening ( $B'_W < 1$ ) the area of high topography defined by the smoothed contour of  $\sim 2,000$  m elevation and bounding faults (Figure 4a), and the central Tibetan Plateau (Figure 5a). Although the irregular geometry makes for a somewhat complex dependence of strain-rate on  $B'_S$ , for  $n = 3$ , setting  $B'_S = 10$  results in strain rates around  $10^3$  times smaller than in an adjoining region where  $B' = 1$ . Setting  $B'_S = 10$  in these regions can almost entirely suppress internal strain; the model calculation is insensitive to further increases of the viscosity coefficient in the strong regions. In addition, altering the elevation threshold to for example, 2,500 m does not change the extent of the weak region appreciably.

### 3. Numerical Simulations and Results

We conduct a comprehensive suite of numerical experiments, aiming to match the key features of the geodetic observations (Table 1) under a fixed set of boundary conditions. We incrementally build up the complexity of models in terms of the number of features employed, with the aim to find the most parsimonious solution that matches the large-scale, systematic patterns of the velocity field. In Case 1, we investigate internal strength variations by involving strong Indian Plate, Tarim, Sichuan, and Alxa-Ordos Basins, a weak area of high topography, and a weak central Tibetan Plateau. In Case 2, we account for displacement discontinuities by explicitly incorporating faults. In each case, we explore the parameter space systematically to obtain a minimum RMS misfit between observations and instantaneous model horizontal velocities.

#### 3.1. Case 1: Lateral Heterogeneity in Viscosity Coefficient

##### 3.1.1. Case 1.1: Rigid India Indenter

In this case, we simulate the convergence of India with Eurasia by embedding a rigid Indian Plate in the otherwise homogeneous model domain (Figure 2a). Doing so allows us to apply the present rotation rate vector for India relative to Eurasia (Section 2.2.2) to the arbitrary southern boundary of the domain, in order to produce the apparent motion of the relatively rigid Indian Plate. The Argand number  $Ar = 0$  gives the minimum RMS misfit (7.1 mm/yr, Figure 2b) subject to the choice of  $n = 3$  and specified boundary conditions. No displacement is allowed on faults but we observe strain concentrations on the syntaxial regions on either end of the Himalayan chain, and also at points on the external boundary of the domain (Figure 2c), where there is an abrupt change in the boundary conditions (Figure 2a). Neither dilatation of high plateau nor clockwise rotation around the EHS is reproduced.

##### 3.1.2. Case 1.2: Embedding Strong Indian Plate, Tarim, Sichuan, and Alxa-Ordos Basins

Based on the coherent displacement patterns of the Indian Plate, Tarim, Sichuan, and Alxa-Ordos Basins observed in GNSS data set, these regions are interpreted to behave as rigid blocks with relatively cold thermal profiles (Craig et al., 2012; Y. Deng & Tesauro, 2016; Jagadeesh & Rai, 2008; Kao et al., 2001; C. Li, van der Hilst, Engdahl, & Burdick, 2008; Mahesh et al., 2012; Rui & Stamps, 2016; Tapponnier & Molnar, 1976; Q. Wang et al., 2001; Yang & Liu, 2002; C.-L. Zhang et al., 2013; P. Zhang & Gan, 2008; Z. Zhang et al., 2010). We set the four regions to have a viscosity coefficient one order of magnitude higher than background ( $B'_S = 10$ ) (Figure 3a). The outlines of the rigid regions are approximated from the surface geomorphology/topography. In this

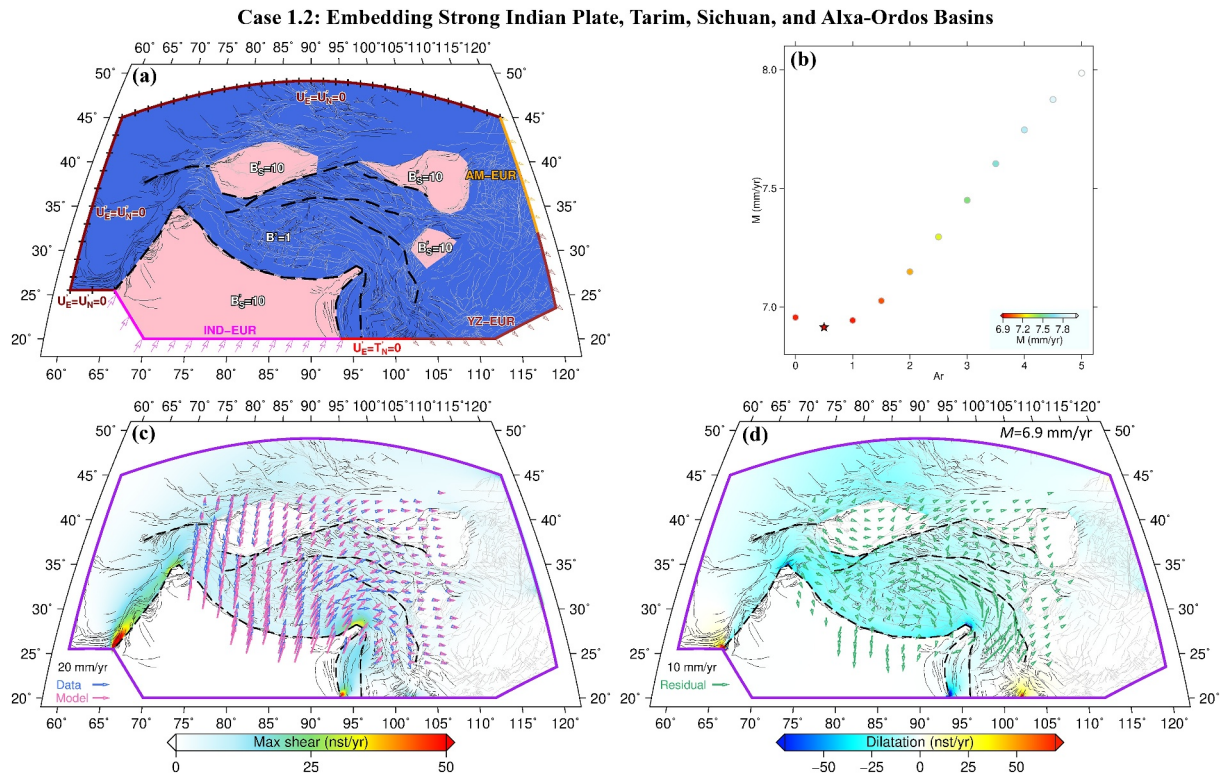


**Figure 3.** Same as Figure 2, but for Case 1.2: embedding strong Indian Plate, Tarim, Sichuan, and Alxa-Ordos Basins.

calculation, the minimum misfit ( $\sim 6.9$  mm/yr) obtained for Argand number 0.5 (Figure 3b) is comparable to Case 1.1. Asymmetric eastward velocity gradient in the western and eastern Tibetan Plateau and clockwise rotation around the EHS are not recovered (Figure 3c). Negligible strain occurs in the interiors of the rigid blocks. Northward displacement rate vectors are still predominant everywhere in the solution domain in contrast to observed eastward rates in the eastern Tibetan Plateau.

### 3.1.3. Case 1.3: Weak Area of High Topography

The lithosphere of the Tibetan Plateau and Tian Shan has been suggested to be relatively thinner, hotter and rheologically weaker than the indenting Indian Plate and the Tarim Basin (Molnar & Tapponnier, 1981; Tapponnier & Molnar, 1979). In this case we explore the effect of weakening these regions of high elevation. We choose the weak region to lie within the smoothed elevation contour of  $\sim 2,000$  m bounded by faults in places (medium blue zone in Figure 4a). The spatial extent broadly corresponds with zones showing slow anomalies according to the seismic tomographic model (e.g., C. Li, van der Hilst, Meltzer, & Engdahl, 2008), suggesting higher temperature, lower density, and reduced strength compared to adjacent regions. We search for an optimal combination of the Argand number and the viscosity coefficient of the weak zone ( $B'_w$ ). A minimum misfit of 5.7 mm/yr was obtained with  $Ar$  of  $\sim 3.5$  and  $B'_w$  of  $\sim 0.4$  (Figure 4b), indicating that gravitational spreading of the plateau plays a more significant role when enabled by weakened thick crust. It can be seen that there is some trade-off between  $Ar$  and  $B'_w$ ; as  $Ar$  increases, a relatively “stronger” weak zone would be required. This model calculation enhances the expression of eastward motion in the eastern Tibetan Plateau (Figures 4c and 6c). Clockwise rotation around the EHS is still missing (Figure 4c). Note that strain becomes concentrated at regions of strength contrast. The high plateau is dilating in this experiment, as the weaker plateau is enabled to flow outward from the region of high GPE. The margins of the plateau show convergence. These patterns are broadly consistent with the geodetically-derived dilatation strain rate field (C. Liu et al., 2024; Wright et al., 2023).

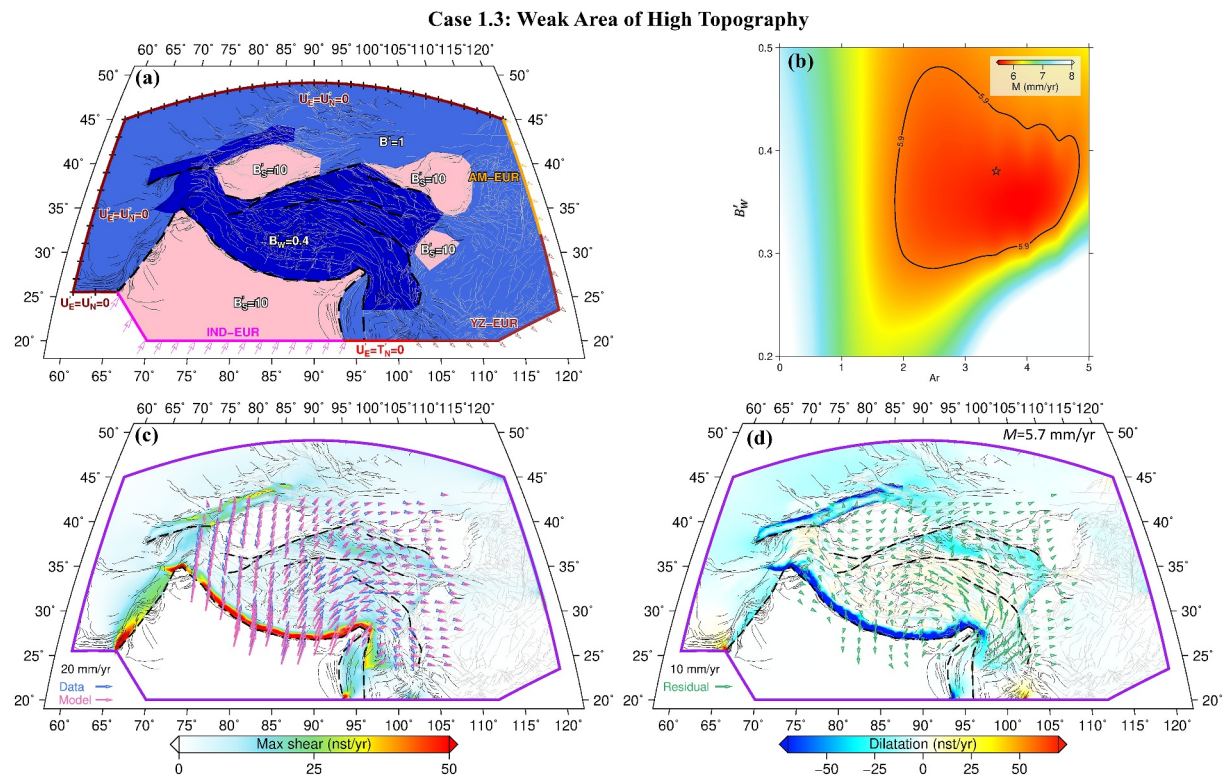


**Figure 4.** (a) Schematic diagram illustrating boundary conditions and model rheological coefficients for Case 1.3: including a weak area of high topography. The weak zone follows the smoothed contour of  $\sim 2,000$  m elevation bounded by faults in places. (b) Misfit as a function of the Argand number and viscosity coefficient of the weak zone. The minimum misfit is marked as a star. Conventions of (c) and (d) are as described in Figure 2.

### 3.1.4. Case 1.4: Further Weakened Central Tibetan Plateau

We note that none of the above experiments can produce the observed long-wavelength increase in eastward velocity across the Tibetan Plateau (Figure 7a). We now include in the model an additional rheologically weak central plateau, which is bounded by the Jinsha Suture-Xianshuihe Fault to the north, the Bangong-Nujiang Suture to the south, and the Lijiang-Xiaojinhe Fault to the east (dark blue zone in Figure 5a). The misfit is dependent on the Argand number, viscosity coefficients of the weak high topographic area ( $B'_W$ ) and central Tibetan Plateau ( $B'_{W2}$ ). The combination of the three parameters (4, 0.4, 0.1, respectively) leads to a minimum misfit of 5.1 mm/yr (Figure 5b), as opposed to 5.7 mm/yr in Case 1.3. This simulation enhances the eastward velocity gradient across the Tibetan Plateau (Figures 5c, 6d, and 7a). Again, the clockwise rotation around the EHS is not reproduced (Figure 5c). The strain rate fields in this calculation are similar to those of Case 1.3, except for additional strain concentration in part of the southeastern plateau where there is a variation in lithospheric strength. The significance of this experiment is that we recover the gradient of eastward velocity across the Tibetan Plateau ( $\sim 20$  mm/yr contrast over  $\sim 1,400$  km distance, compared to  $\sim 10$  mm/yr difference over that distance in Case 1.3, Figure 7a).

## 3.2. Case 2: Allowing Displacements on Selected Major Faults

In Cases 1.3 and 1.4, strain is concentrated at regions of strength contrast (Figures 4c and 5c). As obvious velocity gradients have been observed across major faults in the Tibetan Plateau (Wright et al., 2023; Figure 7), we introduce strain localization on faults by explicitly allowing for displacement discontinuities across the faults in Case 2.

### 3.2.1. Case 2.1: Absence of Weak Zone

We first exclude any weak regions to investigate the impact of fault-resistance coefficients. We take into account the dominant strike-slip motion along major faults (Altyn Tagh, Haiyuan, Kunlun, and Xianshuihe-Xiaojiang

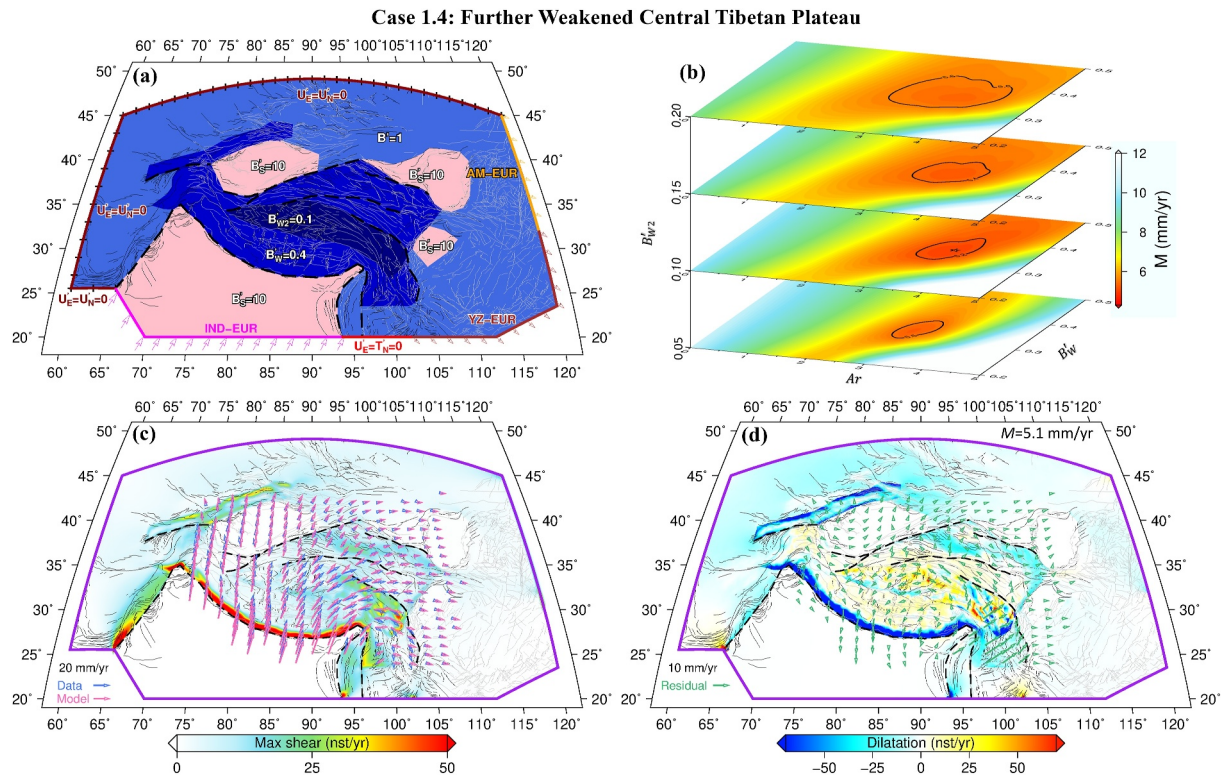


**Figure 5.** (a) Schematic diagram illustrating boundary conditions and model rheological coefficients for Case 1.4: further weakened central Tibetan Plateau. (b) Root mean square misfit as a function of the Argand number, viscosity coefficients of high topographic area ( $B'_{W2}$ ) and central Tibetan Plateau ( $B'_W$ ). In this 3-D parameter space, the minimum misfit of 5.1 mm/yr is found for  $Ar = 4$ ,  $B'_W = 0.4$  and  $B'_{W2} = 0.1$ . Conventions of (c) and (d) are as described in Figure 2.

Faults) by applying a constant strike-parallel fault-resistance coefficient ( $f'_i$ ) along a fault and the prevailing dip-slip movement along the Main Himalayan and Pamir Thrusts by applying a constant strike-perpendicular fault-resistance coefficient ( $f'_n$ ). Given the complex faulting due to the Indo-Burma convergence, we allow both strike-slip and dip-slip motion in the Indo-Burma Ranges and on the Sagaing Fault by applying  $f'_i$  and  $f'_n$  parameters simultaneously. Model faults are delineated as thick black lines in Figure 8a. In this case, we allow  $Ar$  and  $f'_i$  to be free parameters. To maintain the simplicity of the calculations, we begin with a uniform  $f'_i$  and find minor improvements by adjusting  $f'_i$  and/or  $f'_n$  on individual faults by trial and error if required. We obtain a misfit of 4.8 mm/yr with  $Ar$  of  $\sim 1$ . The fault-resistance coefficient  $f'_i = 0$  on major strike-slip faults indicates that the faults can slip freely in strike-parallel direction. On most of the faults, we did not need to reduce  $f'_n$  from the zero slip condition ( $f'_n = inf$ ) but found that misfit was reduced by setting  $f'_n = 0$  for the Sagaing Fault,  $f'_n = 5$  for the Main Pamir Thrust and Indo-Burma Ranges,  $f'_n = 20$  for the Main Himalayan Thrust. This calculation allows discontinuities in the velocity component across faults (Figures 6e and 7) and reproduces the asymmetric eastward velocity gradient across the Tibetan Plateau (Figure 8c). Relative to previous simulations, Case 2.1 predicts a greater rate of clockwise rotation of the Tarim Basin, owing to shear motion allowed on the Altyn Tagh Fault as the basin's southern boundary. The fault-resistance coefficients determine the velocity steps across the faults (Figure 7). Note that geodetic data constrain short-term interseismic elastic strain rates across locked faults, whereas the geodynamic model is predicting long-term velocities and viscous strains averaged over multiple earthquake cycles. To facilitate comparison, we apply a Gaussian filter with a sigma of 15 km to the model velocity field to simulate the effect of a locked elastic lid above the ductile deforming lithosphere before calculating the strain rate fields (Figure S2 in Supporting Information S1). In Case 2.1, strain concentrations on major faults are reproduced (Figure 8c), whereas dilatation of high plateau is missing (Figure 8d). The long-wavelength eastward velocity variation away from major faults is not well captured (Figure 7a).

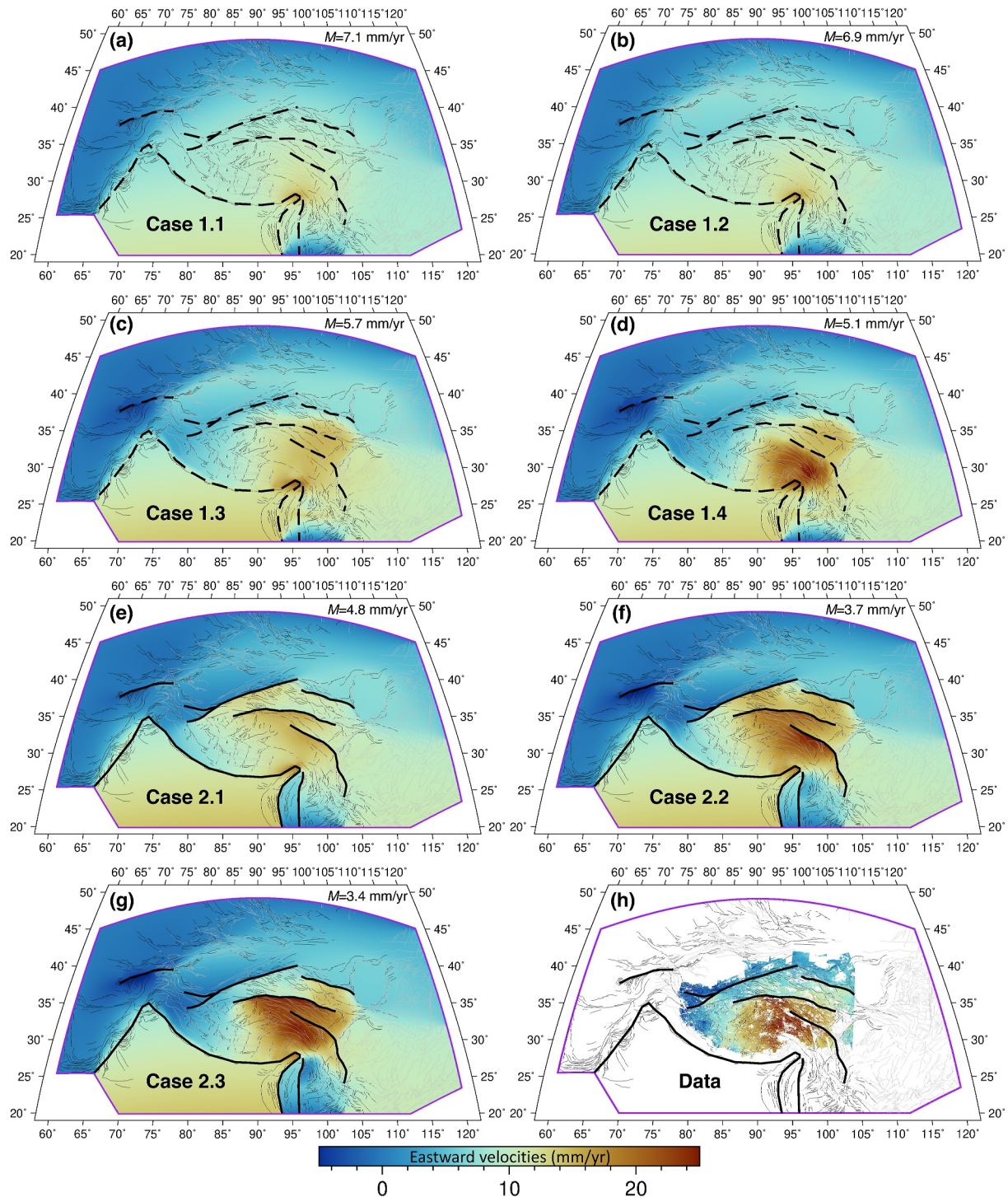


**Figure 6.** (a–g) Model eastward velocity fields for each numerical simulation, as labeled in the text. The root mean square misfit (Equation 5) is indicated in the top right corner of each subplot. (h) Observed eastward velocities (Same as Figure 1a) plotted in the model domain. The deformation field in the entire India-Eurasia collision zone is constrained by the joint inversion of Interferometric Synthetic Aperture Radar (InSAR) and Global Navigation Satellite System (GNSS) data using the *velmap* approach (H. Wang & Wright, 2012). The extent of InSAR-derived eastward velocity field is much smaller than the model domain primarily determined based on plate motions and GNSS coverage. The boundary conditions from plate motions constrain the far-field deformation in the numerical simulations.

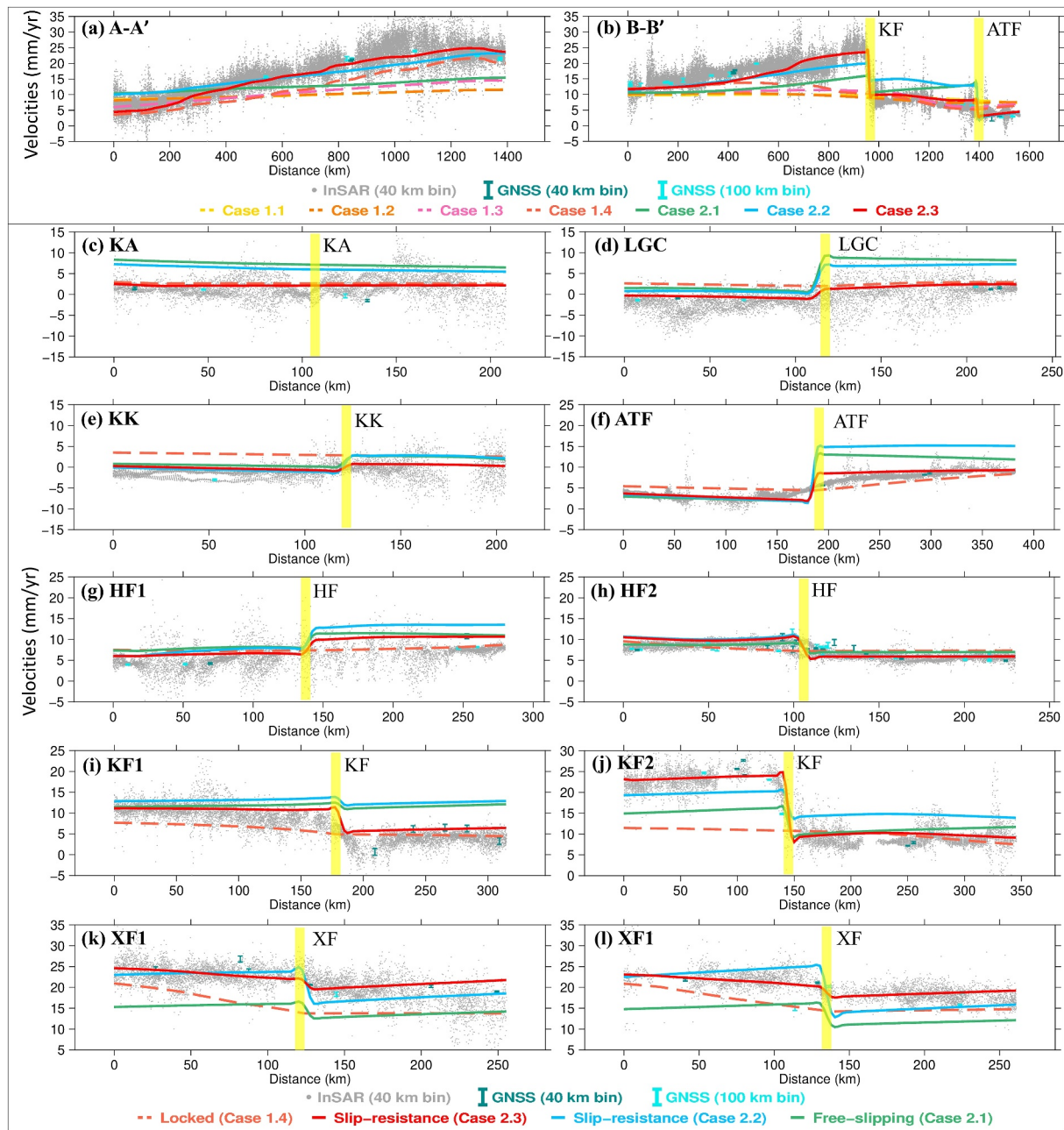


**Figure 7.** Profiles of the east component of velocity whose locations and labels are shown in Figure 1a. We compare observed and model eastward velocities for all the experiments as Interferometric Synthetic Aperture Radar (InSAR) observations are almost insensitive to north-south motion. Velocities from InSAR observations (within 40 km bin) are shown as gray dots. Global Navigation Satellite System (GNSS) observations are shown as dark cyan (40 km bin) and cyan (100 km bin) dots with 1-sigma error bars, respectively (see Text S1 in Supporting Information S1 for more details regarding the GNSS compilation). Yellow bars mark the location of faults. (a) We measure the velocity variation away from major faults along profile A-A', approximately perpendicular to the direction of the India-Eurasia collision. (b) Profile nearly parallel to the direction of the collision. Colored lines represent model velocities for model calculations described in preceding sections of the text, among which cases without faults are shown as dashed lines while cases that allow movement on faults are shown as solid lines. (c–l) Profiles across major strike-slip faults in the Tibetan Plateau showing the effect of the fault-resistance coefficients. Model velocities in cases without faults are shown as red dashed lines ( $f'_i = inf$ , Case 1.4). Green solid lines denote faults that are free-slipping ( $f'_i = 0$ , Case 2.1). Blue solid lines are faults with uniform resistance to slip ( $f'_i = 0.5$ , Case 2.2). Red solid lines represent faults with various resistance to slip (Case 2.3). Faults: KA, Karakoram Fault; LGC, Longmu-Gozha Co Fault; KK, Karakash Fault; ATF, Altyn Tagh Fault; HF, Haiyuan Fault; KF, Kunlun Fault; XF, Xianshuihe-Xiaojiang Fault.

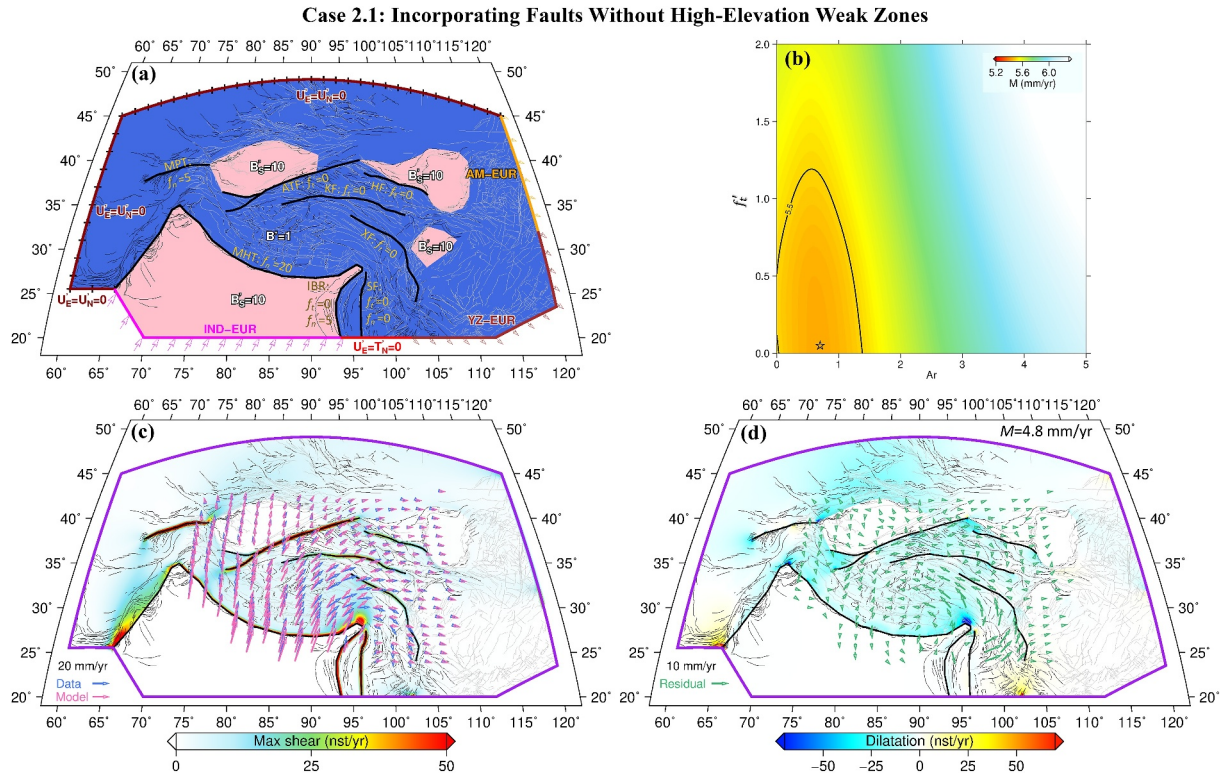


**Figure 8.** (a) Schematic diagram illustrating boundary conditions and internal structures for Case 2.1: incorporating faults without high-elevation weak zones. Thick black lines denote model faults: MPT, Main Pamir Thrust; ATF, Altyn Tagh Fault; HF, Haiyuan Fault; KF, Kunlun Fault; XF, Xianshuihe-Xiaojiang Fault; SF, Sagaing Fault; IBR, Indo-Burma Ranges; MHT, Main Himalayan Thrust.  $f'_t$  and  $f'_n$  are fault-resistance coefficients in tangential and normal directions, respectively. (b) Misfit as a function of the Argand number and fault-resistance coefficient. The best-fit solution has  $Ar \sim 1$ ,  $f'_t = 0$  and  $f'_n = inf$  for all strike-slip faults, except  $f'_n = 0$  for SF,  $f'_n = 5$  for MPT and IBR,  $f'_n = 20$  for MHT, which further reduced the root mean square misfit to 4.8 mm/yr in (d). (c) Model fits (pink arrows) to the sampled observations (blue arrows) derived from joint inversion of Interferometric Synthetic Aperture Radar and Global Navigation Satellite System. The underlying map shows model maximum shear strain rate field for this case. Model faults are shown in thick black lines. (d) Residual vectors, underlain by model dilatation strain rate field.

### 3.2.2. Case 2.2: Embedding Weak Region of High Topography

We now include (Figure 9a) the weak high-elevation areas along with the faults, as described in Section 3.1.3, in attempting to reproduce the dilatation of the high plateau (Case 1.3, Figure 4d, and Table 1). For a given viscosity coefficient of the weak zone ( $B'_W$  of 0.1–0.5), we explore an optimal combination of the Argand number and fault-resistance coefficients. The model favors a  $B'_W$  of 0.3 for the weak zone,  $Ar$  of  $\sim 3$ , and  $f'_t$  of 0.5 for strike-slip faults. We manually modify  $f'_n$  parameters on faults where  $f'_n$  is applied. We obtain a misfit of 3.7 mm/yr, with  $f'_n = 0.5$  for the Sagaing Fault,  $f'_n = 5$  for the Main Pamir Thrust and Indo-Burma Ranges,  $f'_n = inf$  for the Main Himalayan Thrust (no-slip). The weakened plateau appears to accommodate most of the velocity gradient across the Himalayan Thrust, without requiring normal displacement on the Himalayan fault. The weak Tibetan Plateau also enables the eastward motion in the eastern plateau when compared to Case 2.1 (Figures 6e, 6f, 7k, 7l, 8c, and 9c). Clockwise rotation around the EHS is also enhanced, due to the weak plateau with local convergence allowed on the Sagaing Fault and in the Indo-Burma Ranges. This calculation predicts a gentler eastward velocity gradient ( $<15$  mm/yr contrast over a distance of  $\sim 1,400$  km) than observed ( $\sim 20$  mm/yr) (Figure 7a). Other than this, Model 2.2 recovers the rest of the key observations listed in Table 1.

### 3.2.3. Case 2.3: Further Weakened Central Tibetan Plateau

In this case, we present a hybrid model incorporating faults, the weak high elevation regions ( $B'_W$ ), and the further weakened central Tibetan Plateau ( $B'_{W2}$ ), as described in Section 3.1.4. Case 1.4 showed that  $B'_{W2}$  of 0.1 produces the observed smooth, long-wavelength eastward velocity variation across the plateau (Figure 7a). We here search for a best-fit combination of the Argand number, fault-resistance coefficient, and viscosity coefficient of the weak high topographic region ( $B'_W$ ), with  $B'_{W2}$  fixed at 0.1 (Figures 10a and 10b). We start with a uniform  $f'_t$  and make

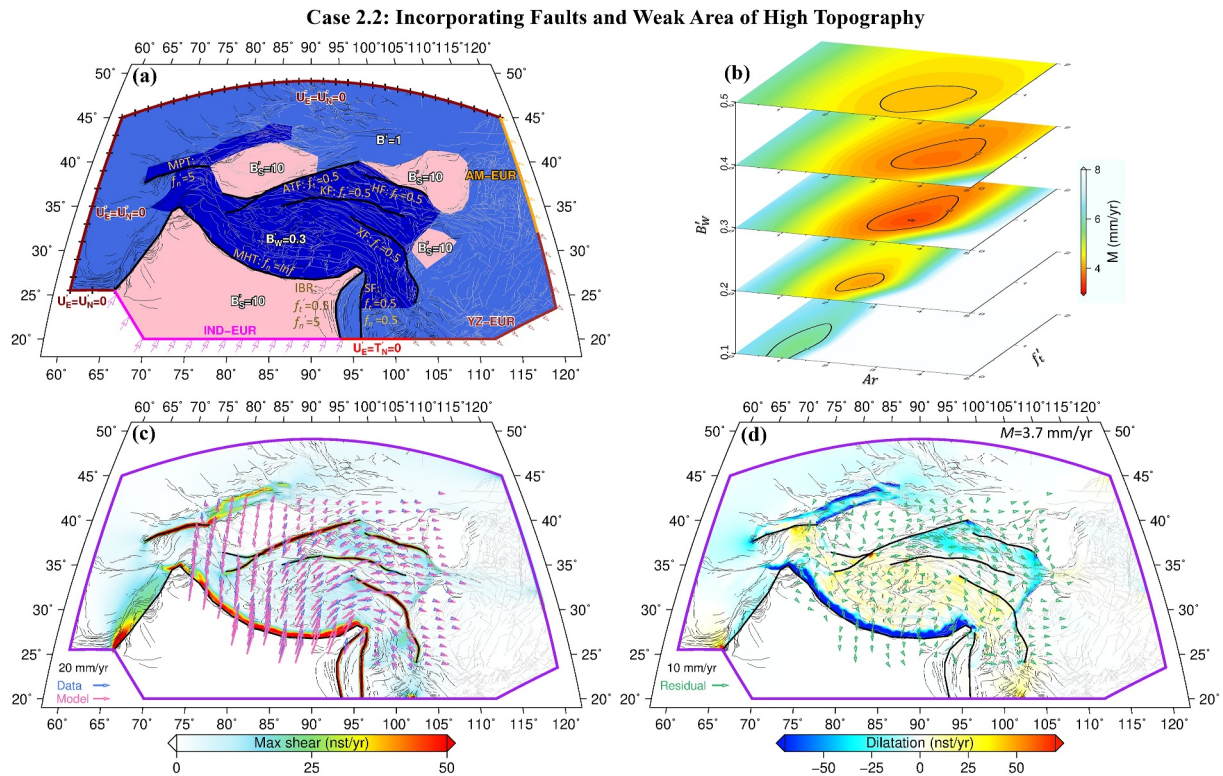


**Figure 9.** (a) Schematic diagram illustrating boundary conditions and internal structures for Case 2.2: incorporating faults and weak region of high topography. The weak zone is bounded approximately by the  $\sim 2,000$  m elevation contour and the major faults. Thick black lines represent model faults: MPT, Main Pamir Thrust; ATF, Altyn Tagh Fault; HF, Haiyuan Fault; KF, Kunlun Fault; XF, Xianshuihe-Xiaojiang Fault; SF, Sagaing Fault; IBR, Indo-Burma Ranges; MHT, Main Himalayan Thrust.  $f'_t$  and  $f'_n$  are fault-resistance coefficients in tangential and normal directions, respectively. (b) Misfit as a function of the Argand number, fault-resistance coefficient, and viscosity coefficient of the weak region. The global minimum misfit occurs at  $B'_w = 0.3$ . The best-fit solution has  $Ar = 3$ ,  $f'_t = 0.5$  and  $f'_n = inf$  for all strike-slip faults, except  $f'_n = 0.5$  for SF,  $f'_n = 5$  for MPT and IBR. Conventions of (c) and (d) are as described in Figure 8.

improvements by adjusting  $f'_t$  and/or  $f'_n$  on individual faults by trial and error. The RMS misfit is reduced to 3.4 mm/yr, subject to the choice of a relatively larger resistance coefficient for the Altyn Tagh Fault ( $f'_t = 2$ ) and the Xianshuihe-Xiaojiang Fault ( $f'_t = 5$ ), and  $f'_t = 0.5$  for the rest of model faults on which strike-slip motion is allowed. In comparison with Case 2.2, the main improvement of Case 2.3 is that the long-wavelength eastward velocity variation has been well captured, with  $\sim 20$  mm/yr increase over  $\sim 1,400$  km (Figure 7a). The model eastward velocity field (Figure 6g) and model-derived strain rate fields (Figures 10c and 10d) show agreement with the geodetic observations (Figures 1a, 1c, and 1d, Wright et al., 2023). This simulation explains all the key features of the India-Eurasia convergence evident in the geodetic observations (Table 1, Figures 6, 7, and 10).

The RMS misfit measures quoted in the preceding sections are defined with respect to the set of vectors shown in Figure 2c. We also tested our preferred model (Case 2.3) against a more comprehensive compilation of GNSS velocities which include data that cover a significantly greater area of the India-Asia collision zone (Figure 1b and Text S1 in Supporting Information S1). Model 2.3 can explain the GNSS observations (Figure 11; Figures S3 and S4 in Supporting Information S1), with a misfit of 3.7 mm/yr. The individual RMS misfit values for each region are 4.3 mm/yr (plateau interior, Figure 11b), 3.2 mm/yr (Tian Shan and northwestern Tibetan Plateau, Figure 11d), 2.3 mm/yr (northeastern Tibetan Plateau, Figure 11f), and 3.6 mm/yr (southeastern Tibetan Plateau, Figure 11h), respectively. The misfit along the Main Himalayan Thrust and the Indo-Burma Ranges is likely due to the simplification of using the faulted TVS model to approximate subduction (Artemieva et al., 2016; Steckler et al., 2008).

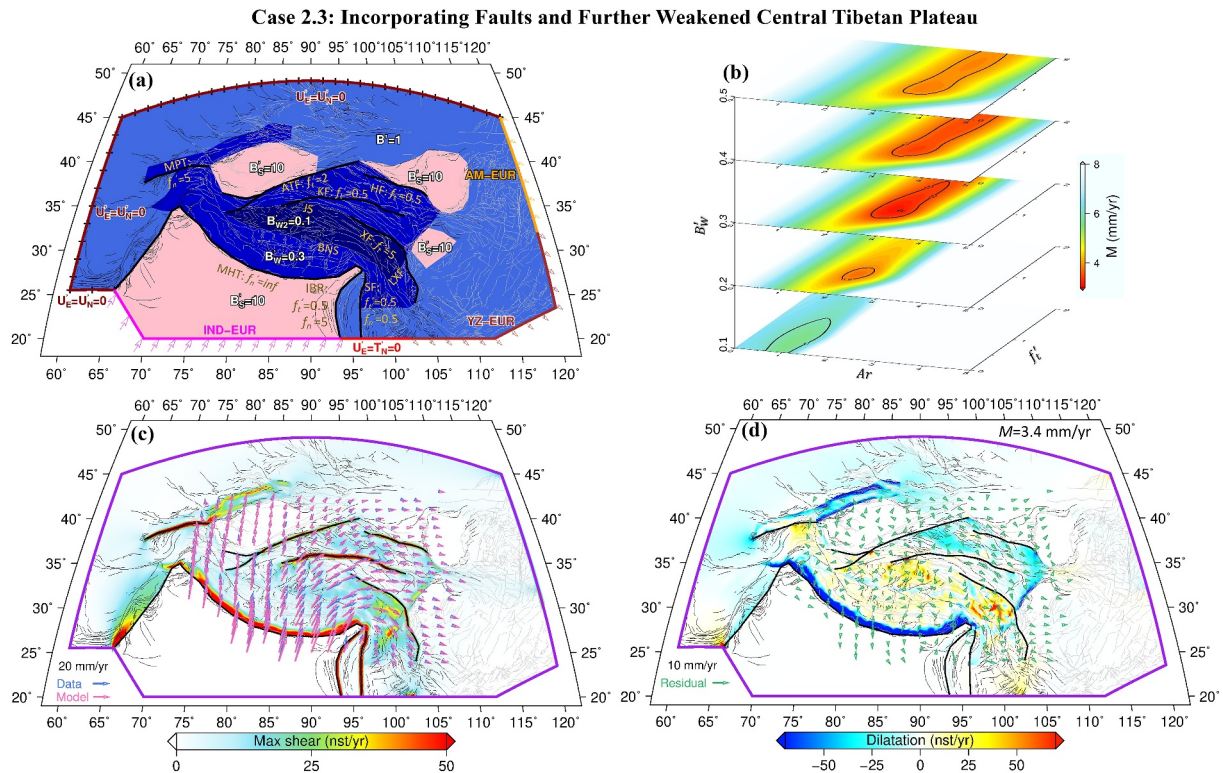


**Figure 10.** Same as Figure 9, but for Case 2.3: incorporating faults and further weakened central Tibetan Plateau. The preferred solution has  $A_r = 3$  and  $B'_w = 0.3$ , with resistance to slip on individual faults determined by adjusting manually from a uniform fault-resistance coefficient for all model faults.

## 4. Discussion

### 4.1. Slip Resistance on Faults Embedded in a Viscous Continuum

A “fault” in the context of the TVS model represents localized strain that is mediated in part by slip on a near-surface fault and by viscous strain of a narrow ductile shear zone at greater depths. Deformation can be generally represented as a continuum influenced by faults. Continuum deformation may comprise both elastic (e.g., earthquakes) and ductile (e.g., folds and shear zones) behavior. The elastic deformation may be neglected when averaged over many fault cycles. We assume the ductile deformation can be described by a non-linear (power-law) viscous rheology. We describe the deformation field in terms of a viscous continuum with faults on which slip is resisted. Barr and Houseman (1996) introduced faults into a viscous medium by applying zero shear stress on the faults. We here generalized their approach using the simplified dynamical assumption that the depth-averaged traction on the fault is proportional to the displacement rate. The key novelty of our faulted TVS models is the ability to more accurately represent the observed velocity field by a combination of continuous distributed deformation and focused strain on major faults. This allows us to investigate the influence of faults on the broader deformation field. In the context of this model, faults can be “locked,” stress-free, or support a traction that is proportional to the slip rate. Importantly, we show that a few faults have a widespread impact beyond the enhanced strain zone around the faults, causing long-wavelength velocity variations (Figures 7a and 7b) as well as discontinuous motion across the faults (Figures 7c–7l).

Given that the model faults in our calculation represent the depth-averaged, time-averaged behavior of a system that undergoes intermittent slip governed by a friction law in the upper 15 km or so, and behaves as a ductile shear zone below that level, there is no direct comparison between the fault resistance coefficient that we use and the parameters that define the frictional behavior of a shallow fault. Because of the time-averaging over multiple earthquake cycles inherent in the formulation of our model, we ignore the cyclic variation of elastic strain that occurs when ductile creep occurs below an upper elastic layer that is locked. In the context of the model, a “locked fault” is one in which the 2-D velocity field is continuous—effectively the fault is then just a marker on the 2-D domain, and we thus draw an important distinction here between the way in which our model fault is “locked”

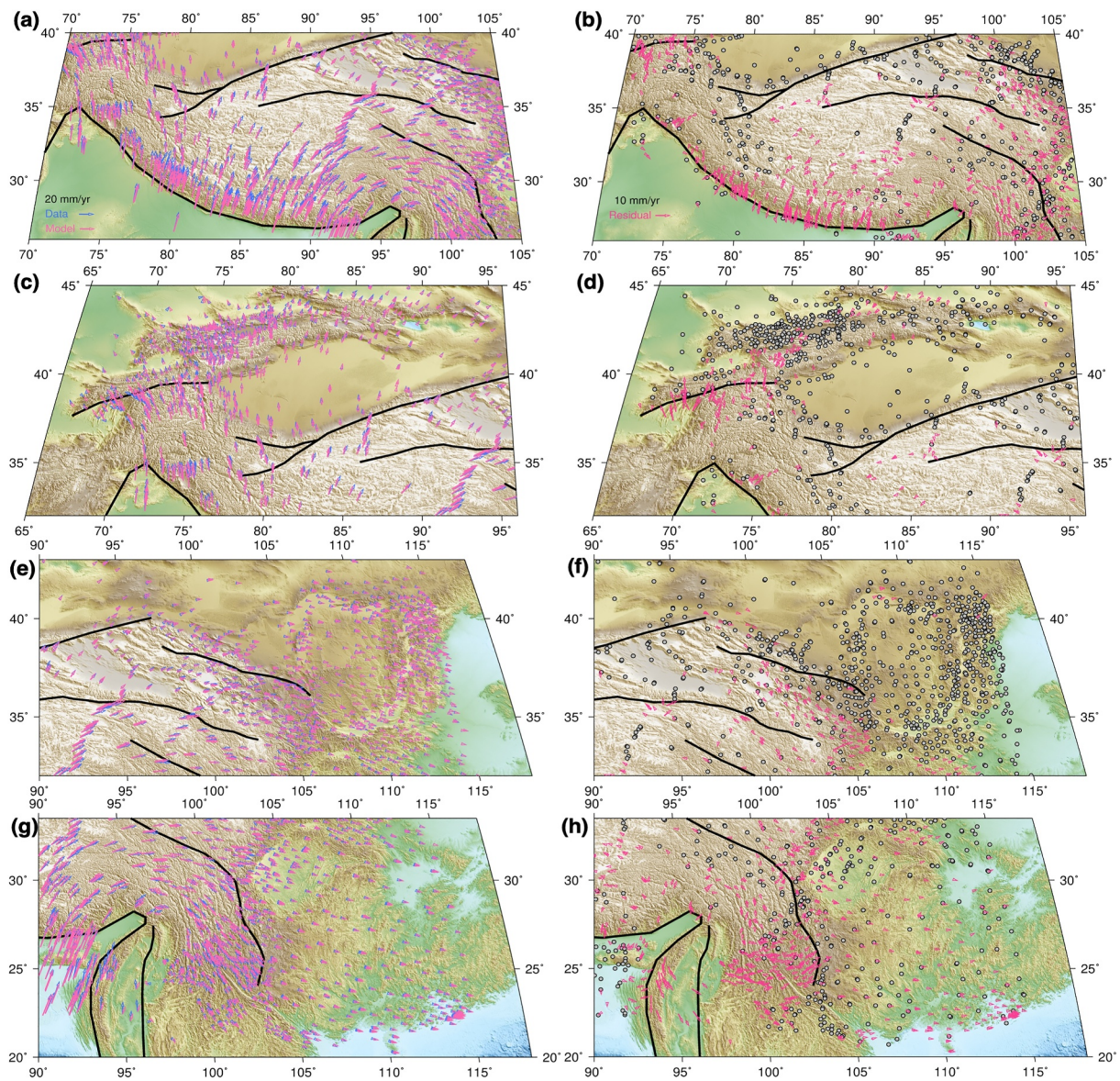


**Figure 11.** Zoomed view of observed (blue arrows) and model (pink arrows) Global Navigation Satellite System (GNSS) velocities for the best-fit solution (i.e., Case 2.3) in plateau interior (a), Tian Shan and northwestern Tibetan Plateau (c), northeastern (e), and southeastern plateau (g). The associated residual vectors are shown as red arrows in (b), (d), (f), and (h). GNSS sites for which the magnitude of the misfit is lower than 2 mm/yr are shown by gray dots. The root mean square misfit values evaluated separately for each region are (b) 4.3 mm/yr, (d) 3.2 mm/yr, (f) 2.3 mm/yr, and (h) 3.6 mm/yr, respectively. The spatial extents of each panel are indicated in Figure 1b. See Text S1 in Supporting Information S1 for more details about the GNSS compilation.

(indicating the absence of both fault and ductile shear zone) and the way in which a frictional fault is locked above a ductile shear zone. In comparing a discontinuous model displacement rate field with the observed geodetic displacement rate field, we take into account the effect of the locked elastic layer by applying a Gaussian filter to the model velocity field, as shown in Figure S2 of Supporting Information S1.

“Locked faults” cannot localize strain unless they coincide with strength-contrast boundaries (e.g., the Xianshuihe-Xiaojiang Fault in Case 1.4, Figures 7k and 7l). Free-slipping faults overestimate the observed velocity steps (e.g., Figures 7d and 7f). The observed velocity gradient across the Kunlun Fault (Figure 7j) might be impacted by the postseismic shallow creeping associated with the 2001  $M_W$  7.8 Kokoxili earthquake; however, strain rates likely decay back to a steady-state focused interseismic strain rate after decades of postseismic transients (Hussain et al., 2018; Ingleby & Wright, 2017).

**Table 2**  
*Comparison of Dynamic Models Predicting the Key Features of the India-Eurasia Collision*

Key observations	2-D modeling				3-D modeling			
	This study (Case 2.3)	England and Houseman (1986)	England and Houseman (1989)	Flesch et al. (2001)	Royden et al. (1997) and F. Shen et al. (2001)	M. Liu and Yang (2003)	Lechmann et al. (2014)	Bischoff and Flesch (2019)
Distributed deformation throughout the India-Eurasia collision zone	✓	✓	✓	✓	✓	✓	✓	✓
Dilatation of high plateau	✓	×	✓	✓	✓	✓	✓	✓
Contraction on the margins of plateau	✓	✓	✓	✓	✓	✓	✓	✓
Smooth, long-wavelength eastward velocity variation away from major faults	✓	–	–	–	–	–	–	–
Strain concentrations on major faults	✓	×	×	×	×	×	✓	✓
Asymmetric eastward velocity gradient across the Tibetan Plateau	✓	–	–	✓	Symmetric	Partly	Symmetric	✓
Clockwise rotation around the EHS	✓	–	–	✓	✓	✓	✓	✓
Clockwise rotation of the Tarim basin	✓	–	–	×	–	×	×	×

Our results show that the best-fit model requires that the resistance to slip on faults may vary with location (Figure 7). Our best-fit model uses a scaled fault-parallel resistance coefficient of  $f_t = 2$  MPa·yr/mm for the Altyn Tagh Fault,  $f_t = 4$  MPa·yr/mm for the Xianshuihe-Xiaojiang Fault, and  $f_t = 0.4$  MPa·yr/mm for the other model faults where strike-slip motion is allowed, subject to the choice of  $Ar = 3$  (Case 2.3). This suggests that there is relatively more resistance to strike-slip movement on the Altyn Tagh Fault and the Xianshuihe-Xiaojiang Fault, meaning higher shear traction is required to produce slip at the same rate. The level of resistance to dip-slip motion on the Main Himalayan Thrust tends to be higher (e.g.,  $f_n = 48$  MPa·yr/mm in Case 2.1, or  $f_n = inf$  meaning “locked” in Cases 2.2 and 2.3). A better constraint on the value of  $f_n$  applicable to the MHT requires further investigation, but allowing localized normal displacement on this boundary would be consistent with geological and seismological observation and may allow residuals along this structure to be reduced.

#### 4.2. Comparison With Previous Dynamic Models of the India-Eurasia Collision

Table 2 shows a compilation of what existing dynamic models of the India-Eurasia collision explain in terms of the key tectonic deformation patterns observed. Our numerical experiments can intrinsically predict large-scale distributed deformation in the India-Eurasia collision zone. The best model (Case 2.3) explains all the key observations from geodesy listed in Table 1 (see Figures 6g, 7, 10, and 11). The laterally homogeneous viscous sheet model (England & Houseman, 1986) does not predict the dilatation of the plateau or focused strain around faults, but lithospheric strength discontinuities cause strain concentration on their boundaries (Bischoff & Flesch, 2019; Dayem, Houseman, & Molnar, 2009; Lechmann et al., 2014; Molnar & Dayem, 2010). We predict nearly E-W extension throughout much of the central-southern Tibetan Plateau and NNW-SSE stretching in the eastern plateau (Figure S5a in Supporting Information S1), consistent with that from geodetic observations (Figure 1c). The vertically-averaged deviatoric stress magnitudes are less than ~40 MPa in the Tibetan Plateau and the Tian Shan region (Figure S5a in Supporting Information S1), in agreement with Flesch et al. (2001). Our model distribution of effective viscosity (Figure S5b in Supporting Information S1) is comparable to those determined by Flesch et al. (2001), M. Liu and Yang (2003), Copley and McKenzie (2007), and Y. Deng and Tesauro (2016). Our results support the findings of a strong ( $10^{24}$  Pa s or greater) Tarim Basin and a weak ( $\sim 10^{22}$  Pa s) Tian Shan

(Figure S5b in Supporting Information S1, Neil & Houseman, 1997). The Tarim Basin appears to behave as a secondary rigid indenter and experiences little internal deformation, but transmits stress and gives rise to local crustal thickening in Tian Shan (Figures 1c, 1d, 10c, and 10d, England & Houseman, 1985; Huangfu et al., 2021; Molnar & Tapponnier, 1975; Neil & Houseman, 1997). We find that a relatively weak ( $10^{22}$ – $10^{23}$  Pa s) high topographic region ( $\sim 2,000$  m) predicts the dilatation of the highest-elevation region of the Tibetan Plateau (Cases 1.3, 1.4, 2.2, and 2.3, Figures 4d, 5d, 9d, and 10d). Thus the rate of E-W extension of the plateau may be explained either by increases in surface elevation (M. Liu & Yang, 2003) and GPE arising from the thermal evolution of thickened continental lithosphere (England & Houseman, 1989), or by a relatively weak Tibetan lithosphere with an average effective viscosity of  $10^{21}$ – $10^{22}$  Pa s (L. Chen et al., 2017; England & Molnar, 1997; Flesch et al., 2001; M. Liu & Yang, 2003).

An additional weaker ( $\sim 10^{21}$  Pa s) central Tibetan Plateau bounded by the Dianzhong Block in the southeastern plateau provides an explanation for the smooth, long-wavelength eastward velocity variation away from major faults (Cases 1.4 and 2.3, Figure 7a). This is consistent with the suggestion that the Dianzhong Block, with higher S-wave velocities and weaker seismic anisotropy compared with the surrounding blocks, obstructs the lithospheric extrusion in the southeastern Tibetan Plateau, causing strain accumulation along the Lijiang-Xiaojinhe Fault (Han et al., 2022) as assumed in Cases 1.4 and 2.3 (Figures 5c and 10c). We also observe a strain-rate concentration along this boundary in the geodetically-derived maximum shear strain rate field, although this is weaker than the prediction in the models, perhaps due to smoothing in the geodetic approach (Figure 1c), or the abrupt change of  $B'$  in the models, which might be smoother in the real Earth. The further weakened central plateau agrees with Y. Deng and Tesauro (2016) who cited high temperatures (high values of the Poisson's ratio, Singh et al., 2015) and high heat flow in this region. The rheological structures calculated by Y. Shi and Cao (2008) and Sun et al. (2013) also show a central plateau region that has a viscosity of 1–2 orders lower than the surrounding region. The widely distributed low-velocity layers, high-conductivity zones, and the presence of silica-rich mélange rock in the central plateau have been interpreted to imply a rheologically weak region (Klemperer, 2006; Y. Li et al., 2013; Nie et al., 2023; Pullen & Kapp, 2014; D. Shi et al., 2004; Wei et al., 2001), although it is debatable to infer the existence of crustal channel flow (Nie et al., 2023) because channel flow of low viscosity crustal material requires a lateral pressure gradient as well as a low viscosity.

High-resolution InSAR data add extra detail to the velocity field in two ways. First, where there is strain on major faults, the InSAR data sharpens and localizes the strain field, providing clarity on which faults are associated with localized strain (Wright et al., 2023; C. Liu et al., 2024). This helps us delineate the extent and geometry of the major faults for our numerical simulations. Second, where the velocity field appears smooth but GNSS measurements are sparse, InSAR confirms the lack of significant strain concentrations. For example, one key observation in our InSAR-based velocity field is the smooth, long-wavelength eastward velocity variation, as depicted in Figure 7a. Incorporation of the high-resolution InSAR velocity field is essential for confirming the absence of focused strain along this profile and helps us infer a further weakened central Tibetan Plateau.

Slip on major faults (Case 2, Figures 8c, 9c, and 10c) and/or lithospheric strength contrasts (e.g., Cases 1.3 and 1.4, Figures 4c and 5c, Lechmann et al., 2014; Bischoff & Flesch, 2019) can produce focused strain. The clockwise rotation of the Tarim block (e.g., Avouac & Tapponnier, 1993; Craig et al., 2012; Z.-K. Shen et al., 2001; J. Zhao et al., 2019) is enhanced by motion on the Altyn Tagh Fault (Case 2, Figures 8c, 9c, and 10c); this rotation was not evident in the experiments of Flesch et al. (2001), M. Liu and Yang (2003), Lechmann et al. (2014), and Bischoff and Flesch (2019) as they did not take account of relative motion on the fault. The clockwise rotation around the EHS was obtained by Bischoff and Flesch (2019) invoking a west-to-east decrease in upper crustal strength. In our numerical simulations, a weak Tibetan Plateau and allowing local convergence to occur on the Sagaing Fault and in the Indo-Burma Ranges, with fault-perpendicular resistance coefficients  $f_n$  of 0.4 and 4 MPa-yr/mm, respectively, allows the displacement pattern around the EHS to be reproduced, and is justified as an approximate characterization of subduction in the Myanmar region (Cases 2.2 and 2.3, Figures 9c and 10c, e.g., Steckler et al., 2008).

### 4.3. Active Faulting and Seismicity

Although the preferred model includes several lithospheric-scale faults on which fault-like displacements are explicitly represented, we also consider that continuous strain within the ductile regions must also be manifest in smaller-scale faulting of the uppermost brittle layer to allow a deformation that is conformable with the

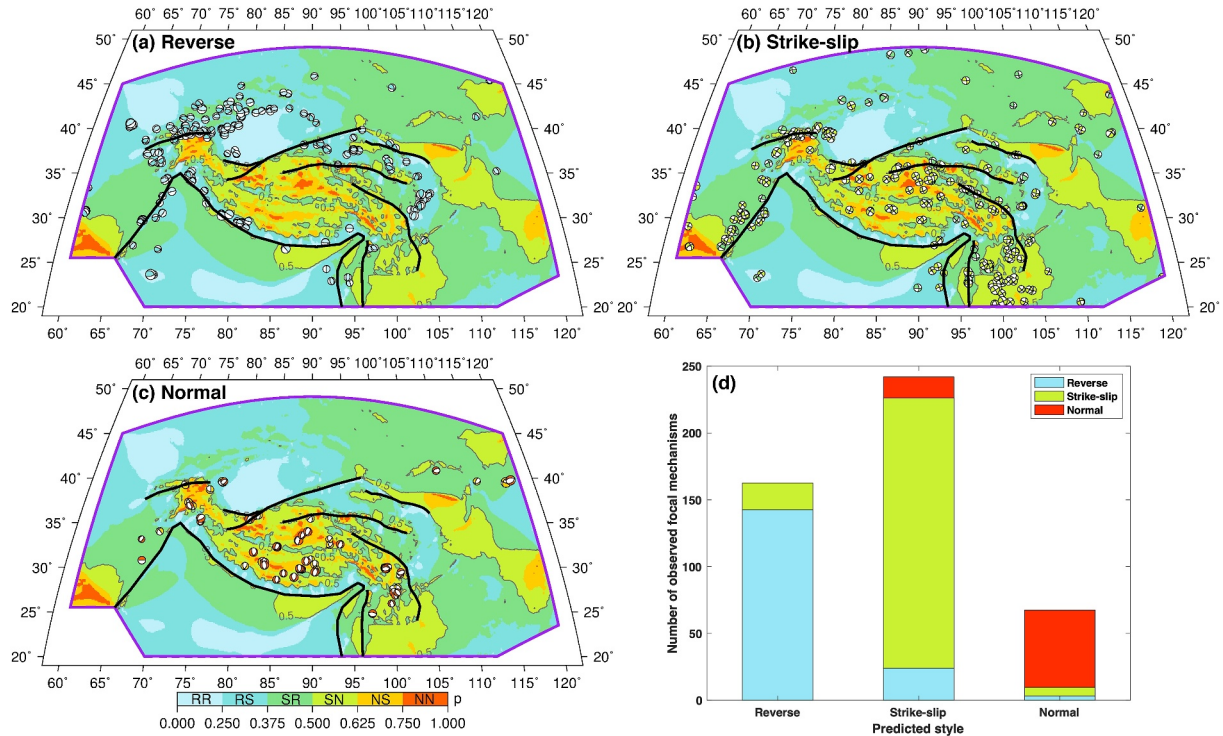


**Figure 12.** Predicted distribution of fault types compared with observed earthquake focal mechanisms (magnitude  $\geq 5.0$ ) from the GCMT catalog (Dziewonski et al., 1981; Ekström et al., 2012). In the two-letter designations, N, S, R, refer to normal, strike-slip, and reverse faulting, with the first letter representing the dominant style of deformation. The  $p = 0.5$  contours are shown as gray lines. Purple lines indicate the boundary of the calculation domain. Thick black lines are model faults. (a) Reverse-faulting earthquakes of the region. (b) Strike-slip-faulting earthquakes. (c) Normal-faulting earthquakes. (d) The earthquakes obtained from the GCMT catalog are classified into three groups based on the orientation of T, B or P axis being nearest to vertical (Álvarez Gómez, 2019); within each group the color coding displays the primary fault-type expected for each earthquake epicenter, based on the  $p$ -value obtained from Model 2.3, using  $p = 0.375$  and  $0.625$  as the range limits.

continuous strain occurring in the ductile layers beneath. To evaluate the style of faulting expected at any given location we consider the triaxial strain rate field as a sum of two double couples aligned with the principal horizontal strain-rate axes ( $\dot{\epsilon}_1$ ) and ( $\dot{\epsilon}_2$ ) (Houseman & England, 1986). The style of faulting that covers the spectrum from normal to strike-slip to reverse faulting can then be described using the parameter  $p$ :

$$p = \frac{3}{4} + \frac{1}{\pi} \arctan\left(\frac{\dot{\epsilon}_2}{\dot{\epsilon}_1}\right) \quad (9)$$

When  $p$  is in the range  $0 \leq p < 0.25$  reverse faulting (RR) is predicted in both principal directions. When  $0.25 \leq p < 0.5$  reverse faulting plus subsidiary strike-slip (RS) or strike-slip plus subsidiary reverse faulting (SR) is predicted, with the transition between RS and SR taking place where  $p = 0.375$ . Pure strike-slip faulting occurs when  $p = 0.5$  and then transitions from strike-slip with subsidiary normal faulting (SN) to normal faulting with subsidiary strike-slip (NS) and from NS to NN take place at  $p = 0.625$  and  $p = 0.75$ , respectively (England et al., 2016; Gordon & Houseman, 2015; Houseman & England, 1986; Walters et al., 2017).

Figure 12 shows the comparison between the predicted distribution of styles of active faulting and the observed earthquake focal mechanisms. The classification of the focal mechanism data was performed using FMC program according to the directions of the P, T, and B Centroid Moment Tensor axes (Álvarez Gómez, 2019). The edges of the plateau are characterized primarily by compressional strain/reverse faulting (Figure 12a). Strike-slip faulting occurs everywhere in the region (Figure 12b). Normal faulting is predicted to dominate in the plateau interior, especially in the southern plateau (Figure 12c). These calculated styles of deformation are in agreement with the distribution of earthquake focal mechanisms (Figure 12d), implying that the faults within the seismogenic upper

crust are taking up strain imposed by the ductile lithosphere. This consistency between model prediction and observation validates a key assumption of negligible vertical gradients of horizontal velocities for the TVS model of the India-Eurasia collision; it is consistent with the force balance required by imposed boundary motions and internal distribution of GPE.

The TVS approach averages the rheological parameters over the thickness of the lithosphere, and thereby ignores the depth variation of those rheological parameters. The vertical partitioning of lithospheric strength is still debated (e.g., Jackson, 2002; Schmalholz et al., 2018; M. Wang et al., 2021). Despite this, our estimate of depth-averaged effective viscosity provides a first-order constraint on the vertical variations of lithospheric strength that constrains the depth-dependence of the viscosity profile. The TVS method also treats the lithosphere as a purely viscous medium, as the elastic strain is not represented in the long-term geological record and may be ignored if the inter-seismic strain rate field is representative of the long-term strain (Barr & Houseman, 1996). The simplicity of the TVS approximation allows us to explore the rheology of the lithosphere and gain insights into the behavior of faults in a viscous continuum and the relationship between active faulting and seismicity.

Although relatively complex, our preferred model is necessarily simplified compared to reality, with assumptions like piece-wise constant viscosity coefficient ( $B'$ ) and constant fault-resistance coefficient ( $f'$ ). Further fine-tuning of these model parameters or adding additional complexity in boundary conditions might produce a more exact fit to data, particularly along the Himalayan arc and the Indo-Burma Ranges, but would probably not change the broad conclusions reached here. However, possible lateral variations of GPE determined by the thermal evolution of the thickened lithosphere could mitigate the requirement for a very weak central Tibetan Plateau. Apparent misfits may also be explained by the 3-D aspects of the collision which are not accounted for in the TVS model (Figures 11b and 11h, Artemieva et al., 2016; Steckler et al., 2008).

## 5. Conclusions

We have shown that two-dimensional dynamic models based on a TVS formulation incorporating discontinuous displacement on major faults can explain the key observations of the India-Eurasia convergence as expressed in the new high-resolution Sentinel-1 InSAR as well as GNSS velocity fields. We conclude that:

1. The balance between gravitational buoyancy-induced stress and viscous stress shapes the deformation field in the India-Asia collision zone; the preferred model fits the combined geodetic observations with an RMS misfit of 3.4 mm/yr and an Argand number of  $\sim 3$ .
2. The observed dilatation strain rate field is explained by the inclusion of a relatively weak region of high topography ( $\sim 2,000$  m) with a depth-averaged effective viscosity of  $10^{22}$ – $10^{23}$  Pa s.
3. A weak central Tibetan Plateau ( $\sim 10^{21}$  Pa s) bounded by the Dianzhong Block enables the smooth, long-wavelength eastward velocity variation away from major faults to be reproduced in the model.
4. Shear resistance to slip ( $f_i = 0.4$ – $4$  MPa·yr/mm) on major faults allows strain concentration on those systems.
5. Clockwise rotation around the EHS is produced by the weak Tibetan Plateau with local convergence allowed along the Indo-Burma Ranges ( $f_n = 4$  MPa·yr/mm) and the Sagaing Fault ( $f_n = 0.4$  MPa·yr/mm), approximately representing subduction in the Myanmar region.

## Data Availability Statement

All interferograms can be accessed through the COMET-LiCSAR portal (<https://comet.nerc.ac.uk/comet-lics-portal/>) and the CEDA archive ([https://data.ceda.ac.uk/neodc/comet/data/licsar\\_products](https://data.ceda.ac.uk/neodc/comet/data/licsar_products)). The derived velocities are available in Fang et al. (2023) (<https://doi.org/10.5281/zenodo.10053499>). The GNSS velocities are compiled from published studies (refer to Text S1 in Supporting Information S1 for more details) and archived in Rollins (2023) (<https://doi.org/10.5281/zenodo.10372924>). The *basil* code, along with example input files for calculations described in this paper, can be found in Houseman (2023) (<https://doi.org/10.5281/zenodo.10052242>, archived on 30 October 2023). The latest version of the *basil* code is continually developed on GitHub and is accessible at <https://github.com/greg-houseman/basil>.

### Acknowledgments

COMET is the UK Natural Environment Research Council (NERC)'s Centre for the Observation and Modeling of Earthquakes, Volcanoes and Tectonics, a partnership between UK Universities and the British Geological Survey. This study was funded by NERC through the "Looking inside the Continents from Space (LiCS)" large Grant to University of Leeds (NE/K010867/1) and COMET National Capability Grants 2014/2019/2021. Jin Fang acknowledges the support through a China Scholarship Council-University of Leeds joint scholarship (202006270022). Tim J. Craig was supported in this work by the Royal Society under University Research Fellowship (URFR1\180088). John R. Elliott acknowledges the funding from Royal Society Fellowship Grant (URFR2\21106) and Royal Society Grant (RF\ERE\210143). We would like to thank Shin-Chan Han, the editor, the associate editor, and three anonymous reviewers for their thorough and constructive comments. We extend gratitude to Chris Rollins for his dedicated efforts in compiling GNSS data. Numerical calculations were undertaken on ARC4, part of the High Performance Computing facilities at the University of Leeds, UK. Figures were produced using the Generic Mapping Tools (GMT) (Wessel et al., 2013) and Matlab.

### References

- Álvarez Gómez, J. A. (2019). FMC—Earthquake focal mechanisms data management, cluster and classification. *SoftwareX*, 9, 299–307. <https://doi.org/10.1016/j.softx.2019.03.008>
- Alvizuri, C., & Hetényi, G. (2019). Source mechanism of a lower crust earthquake beneath the Himalayas and its possible relation to metamorphism. *Tectonophysics*, 769, 128153. <https://doi.org/10.1016/j.tecto.2019.06.023>
- Amante, C., & Eakins, B. W. (2009). ETOPO1 arc-minute global relief model: Procedures, data sources and analysis.
- Artemieva, I., Thybo, H., & Shulgin, A. (2016). Geophysical constraints on geodynamic processes at convergent margins: A global perspective. *Gondwana Research*, 33, 4–23. <https://doi.org/10.1016/j.gr.2015.06.010>
- Ashurkov, S., Serov, M., Zhizherin, V., & Imaev, V. (2018). Present-day deformations in the Upper Amur region from GPS measurements. *Russian Journal of Pacific Geology*, 12(5), 419–428. <https://doi.org/10.1134/S1819714018050020>
- Aung, P. S., Satirapod, C., & Andrei, C.-O. (2016). Sagaing Fault slip and deformation in Myanmar observed by continuous GPS measurements. *Geodesy and Geodynamics*, 7(1), 56–63. <https://doi.org/10.1016/j.geog.2016.03.007>
- Avouac, J.-P., & Tapponnier, P. (1993). Kinematic model of active deformation in central Asia. *Geophysical Research Letters*, 20(10), 895–898. <https://doi.org/10.1029/93GL00128>
- Barman, P., Ray, J. D., Kumar, A., Chowdhury, J., & Mahanta, K. (2016). Estimation of present-day inter-seismic deformation in Kopili fault zone of north-east India using GPS measurements. *Geomatics, Natural Hazards and Risk*, 7(2), 586–599. <https://doi.org/10.1080/19475705.2014.983187>
- Barr, T. D., & Houseman, G. A. (1996). Deformation fields around a fault embedded in a non-linear ductile medium. *Geophysical Journal International*, 125(2), 473–490. <https://doi.org/10.1111/j.1365-246X.1996.tb00012.x>
- Beaumont, C., Jamieson, R. A., Nguyen, M., & Lee, B. (2001). Himalayan tectonics explained by extrusion of a low-viscosity crustal channel coupled to focused surface denudation. *Nature*, 414(6865), 738–742. <https://doi.org/10.1038/414738a>
- Bendick, R., & Flesch, L. (2013). A review of heterogeneous materials and their implications for relationships between kinematics and dynamics in continents. *Tectonics*, 32(4), 980–992. <https://doi.org/10.1002/tect.20058>
- Bischoff, S., & Flesch, L. (2018). Normal faulting and viscous buckling in the Tibetan Plateau induced by a weak lower crust. *Nature Communications*, 9(1), 4952. <https://doi.org/10.1038/s41467-018-07312-9>
- Bischoff, S., & Flesch, L. (2019). Impact of lithospheric strength distribution on India-Eurasia deformation from 3-D geodynamic models. *Journal of Geophysical Research: Solid Earth*, 124(1), 1084–1105. <https://doi.org/10.1029/2018JB015704>
- Bisht, H., Kotlia, B. S., Kumar, K., Dumka, R. K., Taloor, A. K., & Upadhyay, R. (2021). GPS derived crustal velocity, tectonic deformation and strain in the Indian Himalayan arc. *Quaternary International*, 575, 141–152. <https://doi.org/10.1016/j.quaint.2020.04.028>
- Brace, W. F., & Kohlstedt, D. L. (1980). Limits on lithospheric stress imposed by laboratory experiments. *Journal of Geophysical Research*, 85(B11), 6248–6252. <https://doi.org/10.1029/JB085iB11p06248>
- Bürgmann, R., & Dresen, G. (2008). Rheology of the lower crust and upper mantle: Evidence from rock mechanics, geodesy, and field observations. *Annual Review of Earth and Planetary Sciences*, 36(1), 531–567. <https://doi.org/10.1146/annurev.earth.36.031207.124326>
- Chen, L., Capitanio, F. A., Liu, L., & Gerya, T. V. (2017). Crustal rheology controls on the Tibetan plateau formation during India-Asia convergence. *Nature Communications*, 8(1), 15992. <https://doi.org/10.1038/ncomms15992>
- Chen, Q., Freymueller, J. T., Wang, Q., Yang, Z., Xu, C., & Liu, J. (2004). A deforming block model for the present-day tectonics of Tibet. *Journal of Geophysical Research*, 109(B1), B01403. <https://doi.org/10.1029/2002JB002151>
- Clark, M. K., & Royden, L. H. (2000). Topographic ooze: Building the eastern margin of Tibet by lower crustal flow. *Geology*, 28(8), 703–706. [https://doi.org/10.1130/0091-7613\(2000\)28<703:TOBTEM>2.0.CO;2](https://doi.org/10.1130/0091-7613(2000)28<703:TOBTEM>2.0.CO;2)
- Copley, A., Avouac, J.-P., & Wernicke, B. P. (2011). Evidence for mechanical coupling and strong Indian lower crust beneath southern Tibet. *Nature*, 472(7341), 79–81. <https://doi.org/10.1038/nature09926>
- Copley, A., & McKenzie, D. (2007). Models of crustal flow in the India-Asia collision zone. *Geophysical Journal International*, 169(2), 683–698. <https://doi.org/10.1111/j.1365-246X.2007.03343.x>
- Craig, T. J., Copley, A., & Jackson, J. (2012). Thermal and tectonic consequences of India underthrusting Tibet. *Earth and Planetary Science Letters*, 353, 231–239. <https://doi.org/10.1016/j.epsl.2012.07.010>
- Crupa, W. E., Khan, S. D., Huang, J., Khan, A. S., & Kasi, A. (2017). Active tectonic deformation of the western Indian plate boundary: A case study from the Chamam Fault System. *Journal of Asian Earth Sciences*, 147, 452–468. <https://doi.org/10.1016/j.jseaes.2017.08.006>
- Dal Zilio, L., Hetényi, G., Hubbard, J., & Bollinger, L. (2021). Building the Himalaya from tectonic to earthquake scales. *Nature Reviews Earth & Environment*, 2(4), 251–268. <https://doi.org/10.1038/s43017-021-00143-1>
- Dayem, K. E., Houseman, G. A., & Molnar, P. (2009). Localization of shear along a lithospheric strength discontinuity: Application of a continuous deformation model to the boundary between Tibet and the Tarim Basin. *Tectonics*, 28(3), TC3002. <https://doi.org/10.1029/2008TC002264>
- Dayem, K. E., Molnar, P., Clark, M. K., & Houseman, G. A. (2009). Far-field lithospheric deformation in Tibet during continental collision. *Tectonics*, 28(6), TC6005. <https://doi.org/10.1029/2008TC002344>
- DeMets, C., Gordon, R. G., & Argus, D. F. (2010). Geologically current plate motions. *Geophysical Journal International*, 181(1), 1–80. <https://doi.org/10.1111/j.1365-246X.2009.04491.x>
- DeMets, C., Merkouriev, S., & Jade, S. (2020). High-resolution reconstructions and GPS estimates of India–Eurasia and India–Somalia plate motions: 20 Ma to the present. *Geophysical Journal International*, 220(2), 1149–1171. <https://doi.org/10.1093/gji/ggz508>
- Deng, Q., Zhang, P.-Z., Ran, Y.-K., Yang, X., Min, W., & Chen, L.-C. (2003). Active tectonics and earthquake activities in China. *Earth Science Frontiers*, 10(S1), 66–73.
- Deng, Y., & Tesauro, M. (2016). Lithospheric strength variations in Mainland China: Tectonic implications. *Tectonics*, 35(10), 2313–2333. <https://doi.org/10.1002/2016TC004272>
- Devachandra, M., Kundu, B., Catherine, J., Kumar, A., & Gahalaut, V. K. (2014). Global positioning system (GPS) measurements of crustal deformation across the frontal eastern Himalayan syntaxis and seismic-hazard assessment. *Bulletin of the Seismological Society of America*, 104(3), 1518–1524. <https://doi.org/10.1785/0120130290>
- Diao, F., Xiong, X., Wang, R., Walter, T. R., Wang, Y., & Wang, K. (2019). Slip rate variation along the Kunlun fault (Tibet): Results from new GPS observations and a viscoelastic earthquake-cycle deformation model. *Geophysical Research Letters*, 46(5), 2524–2533. <https://doi.org/10.1029/2019GL081940>
- Dumka, R. K., Kotlia, B. S., Kothiyari, G. C., Paikrey, J., & Dimri, S. (2018). Detection of high and moderate crustal strain zones in Uttarakhand Himalaya, India. *Acta Geodaetica et Geophysica*, 53(3), 503–521. <https://doi.org/10.1007/s40328-018-0226-z>

- Dumka, R. K., Kotlia, B. S., Kumar, K., Satyal, G. S., & Joshi, L. M. (2014). Crustal deformation revealed by GPS in Kumaun Himalaya, India. *Journal of Mountain Science*, *11*(1), 41–50. <https://doi.org/10.1007/s11629-012-2552-x>
- Duvall, A. R., Clark, M. K., Kirby, E., Farley, K. A., Craddock, W. H., Li, C., & Yuan, D.-Y. (2013). Low-temperature thermochronometry along the Kunlun and Haiyuan Faults, NE Tibetan Plateau: Evidence for kinematic change during late-stage orogenesis. *Tectonics*, *32*(5), 1190–1211. <https://doi.org/10.1002/tect.20072>
- Dziewonski, A. M., Chou, T. A., & Woodhouse, J. H. (1981). Determination of earthquake source parameters from waveform data for studies of global and regional seismicity. *Journal of Geophysical Research*, *86*(B4), 2825–2852. <https://doi.org/10.1029/JB086iB04p02825>
- Ekström, G., Nettles, M., & Dziewoński, A. (2012). The global CMT project 2004–2010: Centroid-moment tensors for 13,017 earthquakes. *Physics of the Earth and Planetary Interiors*, *200*, 1–9. <https://doi.org/10.1016/j.pepi.2012.04.002>
- England, P., & Houseman, G. (1985). Role of lithospheric strength heterogeneities in the tectonics of Tibet and neighbouring regions. *Nature*, *315*(6017), 297–301. <https://doi.org/10.1038/315297a0>
- England, P., & Houseman, G. (1986). Finite strain calculations of continental deformation: 2. Comparison with the India-Asia Collision Zone. *Journal of Geophysical Research*, *91*(B3), 3664–3676. <https://doi.org/10.1029/JB091iB03p03664>
- England, P., & Houseman, G. (1989). Extension during continental convergence, with application to the Tibetan Plateau. *Journal of Geophysical Research*, *94*(B12), 17561–17579. <https://doi.org/10.1029/JB094iB12p17561>
- England, P., Houseman, G., & Nocquet, J.-M. (2016). Constraints from GPS measurements on the dynamics of deformation in Anatolia and the Aegean. *Journal of Geophysical Research: Solid Earth*, *121*(12), 8888–8916. <https://doi.org/10.1002/2016JB013382>
- England, P., & McKenzie, D. (1982). A thin viscous sheet model for continental deformation. *Geophysical Journal International*, *70*(2), 295–321. <https://doi.org/10.1111/j.1365-246X.1982.tb04969.x>
- England, P., & Molnar, P. (1997). Active deformation of Asia: From kinematics to dynamics. *Science*, *278*(5338), 647–650. <https://doi.org/10.1126/science.278.5338.647>
- England, P., & Molnar, P. (2005). Late Quaternary to decadal velocity fields in Asia. *Journal of Geophysical Research*, *110*(B12), B12401. <https://doi.org/10.1029/2004JB003541>
- England, P., & Molnar, P. (2015). Rheology of the lithosphere beneath the central and western Tien Shan. *Journal of Geophysical Research: Solid Earth*, *120*(5), 3803–3823. <https://doi.org/10.1002/2014JB011733>
- Fang, J., Houseman, G. A., Wright, T. J., Evans, L. A., Craig, T. J., Elliott, J. R., & Hooper, A. (2023). The dynamics of the India-Eurasia collision: Faulted viscous continuum models constrained by high-resolution Sentinel-1 InSAR and GNSS velocities [Dataset]. *Zenodo*. <https://doi.org/10.5281/zenodo.10053499>
- Fazilova, D., Ehgamberdiev, S., & Kuzin, S. (2018). Application of time series modeling to a national reference frame realization. *Geodesy and Geodynamics*, *9*(4), 281–287. <https://doi.org/10.1016/j.geog.2018.04.003>
- Flesch, L., Bendick, R., & Bischoff, S. (2018). Limitations on inferring 3D architecture and dynamics from surface velocities in the India-Eurasia collision zone. *Geophysical Research Letters*, *45*(3), 1379–1386. <https://doi.org/10.1002/2017GL076503>
- Flesch, L., Haines, A. J., & Holt, W. E. (2001). Dynamics of the India-Eurasia collision zone. *Journal of Geophysical Research*, *106*(B8), 16435–16460. <https://doi.org/10.1029/2001JB000208>
- Froehling, E., & Szeliga, W. (2016). GPS constraints on interplate locking within the Makran subduction zone. *Geophysical Journal International*, *205*(1), 67–76. <https://doi.org/10.1093/gji/eggw001>
- Gahalaut, V. K., Gahalaut, K., Catherine, J. K., Sreejith, K., Agrawal, R., Yadav, R. K., et al. (2018). Geodetic constraints on tectonic and anthropogenic deformation and seismogenesis of Koyna–Warna region, India. *Bulletin of the Seismological Society of America*, *108*(5B), 2933–2942. <https://doi.org/10.1785/0120170373>
- Gahalaut, V. K., Gahalaut, K., Dumka, R. K., Chaudhury, P., & Yadav, R. K. (2019). Geodetic evidence of high compression across seismically active Kachchh paleorift, India. *Tectonics*, *38*(8), 3097–3107. <https://doi.org/10.1029/2019TC005496>
- Gan, W., Molnar, P., Zhang, P., Xiao, G., Liang, S., Zhang, K., et al. (2021). Initiation of clockwise rotation and eastward transport of southeastern Tibet inferred from deflected fault traces and GPS observations. *GSA Bulletin*, *134*(5–6), 1129–1142. <https://doi.org/10.1130/B36069.1>
- Garthwaite, M. C., & Houseman, G. A. (2011). Validity of the thin viscous sheet approximation in models of continental collision. *Journal of Geophysical Research*, *116*(B2), B02404. <https://doi.org/10.1029/2010JB007770>
- Gautam, P. K., Gahalaut, V., Prajapati, S. K., Kumar, N., Yadav, R. K., Rana, N., & Dabral, C. P. (2017). Continuous GPS measurements of crustal deformation in Garhwal-Kumaun Himalaya. *Quaternary International*, *462*, 124–129. <https://doi.org/10.1016/j.quaint.2017.05.043>
- Ge, W.-P., Molnar, P., Shen, Z.-K., & Li, Q. (2015). Present-day crustal thinning in the southern and northern Tibetan Plateau revealed by GPS measurements. *Geophysical Research Letters*, *42*(13), 5227–5235. <https://doi.org/10.1002/2015GL064347>
- Godin, L., Grujic, D., Law, R., & Searle, M. (2006). Channel flow, ductile extrusion and exhumation in continental collision zones: An introduction. *Geological Society, London, Special Publications*, *268*(1), 1–23. <https://doi.org/10.1144/GSL.SP.2006.268.01.01>
- Goetze, C., Poirier, J. P., Kelly, A., Cook, A. H., & Greenwood, G. W. (1978). The mechanisms of creep in olivine. *Philosophical Transactions of the Royal Society of London. Series A, Mathematical and Physical Sciences*, *288*(1350), 99–119. <https://doi.org/10.1098/rsta.1978.0008>
- Gordon, R. G., & Houseman, G. A. (2015). Deformation of Indian Ocean lithosphere: Evidence for a highly nonlinear rheological law. *Journal of Geophysical Research: Solid Earth*, *120*(6), 4434–4449. <https://doi.org/10.1002/2015JB011993>
- Grujic, D., Hollister, L. S., & Parrish, R. R. (2002). Himalayan metamorphic sequence as an orogenic channel: Insight from Bhutan. *Earth and Planetary Science Letters*, *198*(1–2), 177–191. [https://doi.org/10.1016/S0012-821X\(02\)00482-X](https://doi.org/10.1016/S0012-821X(02)00482-X)
- Guo, R., Zheng, Y., Tian, W., Xu, J., & Zhang, W. (2018). Locking status and earthquake potential hazard along the middle-south Xianshuihe fault. *Remote Sensing*, *10*(12), 2048. <https://doi.org/10.3390/rs10122048>
- Gupta, T. D., Riguzzi, F., Dasgupta, S., Mukhopadhyay, B., Roy, S., & Sharma, S. (2015). Kinematics and strain rates of the Eastern Himalayan Syntaxis from new GPS campaigns in Northeast India. *Tectonophysics*, *655*, 15–26. <https://doi.org/10.1016/j.tecto.2015.04.017>
- Haines, J., & Sutherland, R. (2018). A faulted thin-sheet model of plate boundary deformation that fits observations. *Journal of Geophysical Research: Solid Earth*, *123*(10), 9162–9185. <https://doi.org/10.1029/2018JB015466>
- Han, C., Huang, Z., Hao, S., Wang, L., Xu, M., & Hammond, J. O. S. (2022). Restricted lithospheric extrusion in the SE Tibetan Plateau: Evidence from anisotropic Rayleigh-wave tomography. *Earth and Planetary Science Letters*, *598*, 117837. <https://doi.org/10.1016/j.epsl.2022.117837>
- Hirschberg, H., & Sutherland, R. (2022). A kinematic model of Quaternary fault slip rates and distributed deformation at the New Zealand plate boundary. *Journal of Geophysical Research: Solid Earth*, *127*(11), e2022JB024828. <https://doi.org/10.1029/2022JB024828>
- Holt, W. E. (2000). Correlated crust and mantle strain fields in Tibet. *Geology*, *28*(1), 67–70. [https://doi.org/10.1130/0091-7613\(2000\)28\(67:CCAMSF\)2.0.CO;2](https://doi.org/10.1130/0091-7613(2000)28(67:CCAMSF)2.0.CO;2)
- Houseman, G. (2023). greg-houseman/basil: Basil (v1.7.6a) [Software]. *Zenodo*. <https://doi.org/10.5281/zenodo.10052242>
- Houseman, G., Barr, T., & Evans, L. (2008). Basil: Stress and deformation in a viscous material (Ch 3.8, pp 77–85). In P. Bons, D. Koehn, & M. Jessell (Eds.), *Microdynamics Simulation. Lecture Notes in Earth Sciences* (Vol. 106). Springer.

- Houseman, G., & England, P. (1986). Finite strain calculations of continental deformation: 1. Method and general results for convergent zones. *Journal of Geophysical Research*, *91*(B3), 3651–3663. <https://doi.org/10.1029/JB091iB03p03651>
- Houseman, G., England, P., & Evans, L. (2023). Combining faulting and ductile deformation in long-term models of continental deformation. In *EGU General Assembly Conference Abstracts* (p. EGU23-4753). <https://doi.org/10.5194/egusphere-egu23-4753>
- Huangfu, P., Li, Z.-H., Zhang, K.-J., Fan, W., Zhao, J., & Shi, Y. (2021). India-Tarim lithospheric mantle collision beneath western Tibet controls the Cenozoic building of Tian Shan. *Geophysical Research Letters*, *48*(14), e2021GL094561. <https://doi.org/10.1029/2021GL094561>
- Hussain, E., Wright, T. J., Walters, R. J., Bekaert, D. P., Lloyd, R., & Hooper, A. (2018). Constant strain accumulation rate between major earthquakes on the North Anatolian Fault. *Nature Communications*, *9*(1), 1392. <https://doi.org/10.1038/s41467-018-03739-2>
- Ingleby, T., & Wright, T. (2017). Omori-like decay of postseismic velocities following continental earthquakes. *Geophysical Research Letters*, *44*(7), 3119–3130. <https://doi.org/10.1002/2017GL072865>
- Jackson, J. (2002). Strength of the continental lithosphere: Time to abandon the jelly sandwich? *Geological Society of America Today*, *12*(9), 4–10. [https://doi.org/10.1130/1052-5173\(2002\)012<0004:SOTCLT>2.0.CO;2](https://doi.org/10.1130/1052-5173(2002)012<0004:SOTCLT>2.0.CO;2)
- Jade, S., Mir, R. R., Vivek, C. G., Shringeshwara, T., Parvez, I., Chandra, R., et al. (2020). Crustal deformation rates in Kashmir valley and adjoining regions from continuous GPS measurements from 2008 to 2019. *Scientific Reports*, *10*(1), 17927. <https://doi.org/10.1038/s41598-020-74776-5>
- Jade, S., Mukul, M., Gaur, V., Kumar, K., Shringeshwar, T., Satyal, G., et al. (2014). Contemporary deformation in the Kashmir–Himachal, Garhwal and Kumaon Himalaya: Significant insights from 1995–2008 GPS time series. *Journal of Geodesy*, *88*(6), 539–557. <https://doi.org/10.1007/s00190-014-0702-3>
- Jade, S., Raghavendra Rao, H., Vijayan, M., Gaur, V., Bhatt, B., Kumar, K., et al. (2011). GPS-derived deformation rates in northwestern Himalaya and Ladakh. *International Journal of Earth Sciences*, *100*(6), 1293–1301. <https://doi.org/10.1007/s00531-010-0532-3>
- Jade, S., Shringeshwara, T., Kumar, K., Choudhury, P., Dumka, R. K., & Bhu, H. (2017). India plate angular velocity and contemporary deformation rates from continuous GPS measurements from 1996 to 2015. *Scientific Reports*, *7*(1), 11439. <https://doi.org/10.1038/s41598-017-11697-w>
- Jagadeesh, S., & Rai, S. S. (2008). Thickness, composition, and evolution of the Indian Precambrian crust inferred from broadband seismological measurements. *Precambrian Research*, *162*(1), 4–15. <https://doi.org/10.1016/j.precamres.2007.07.009>
- Jiao, L., Tapponnier, P., Donzé, F.-V., Scholtès, L., Gaudemer, Y., & Xu, X. (2023). Discrete element modeling of Southeast Asia's 3D lithospheric deformation during the Indian collision. *Journal of Geophysical Research: Solid Earth*, *128*(1), e2022JB025578. <https://doi.org/10.1029/2022JB025578>
- Jouanne, F., Awan, A., Pêcher, A., Kausar, A., Mugnier, J., Khan, I., et al. (2014). Present-day deformation of northern Pakistan from Salt Ranges to Karakorum Ranges. *Journal of Geophysical Research: Solid Earth*, *119*(3), 2487–2503. <https://doi.org/10.1002/2013JB010776>
- Kao, H., Gao, R., Rau, R.-J., Shi, D., Chen, R.-Y., Guan, Y., & Wu, F. T. (2001). Seismic image of the Tarim basin and its collision with Tibet. *Geology*, *29*(7), 575–578. [https://doi.org/10.1130/0091-7613\(2001\)029<0575:SIOTTB>2.0.CO;2](https://doi.org/10.1130/0091-7613(2001)029<0575:SIOTTB>2.0.CO;2)
- Karato, S.-I., Paterson, M. S., & FitzGerald, J. D. (1986). Rheology of synthetic olivine aggregates: Influence of grain size and water. *Journal of Geophysical Research*, *91*(B8), 8151–8176. <https://doi.org/10.1029/JB091iB08p08151>
- Kelemen, P. B., & Dick, H. J. B. (1995). Focused melt flow and localized deformation in the upper mantle: Juxtaposition of replacive dunite and ductile shear zones in the Josephine peridotite, SW Oregon. *Journal of Geophysical Research*, *100*(B1), 423–438. <https://doi.org/10.1029/94JB02063>
- Kirby, S. H., & Kronenberg, A. K. (1987). Rheology of the lithosphere: Selected topics. *Reviews of Geophysics*, *25*(6), 1219–1244. <https://doi.org/10.1029/RG025i006p01219>
- Klemperer, S. L. (2006). Crustal flow in Tibet: Geophysical evidence for the physical state of Tibetan lithosphere, and inferred patterns of active flow. *Geological Society, London, Special Publications*, *268*(1), 39–70. <https://doi.org/10.1144/GSL.SP.2006.268.01.03>
- Kreemer, C., Blewitt, G., & Klein, E. C. (2014). A geodetic plate motion and Global Strain Rate Model. *Geochemistry, Geophysics, Geosystems*, *15*(10), 3849–3889. <https://doi.org/10.1002/2014GC005407>
- Kundu, B., Yadav, R. K., Bali, B. S., Chowdhury, S., & Gahalaut, V. (2014). Oblique convergence and slip partitioning in the NW Himalaya: Implications from GPS measurements. *Tectonics*, *33*(10), 2013–2024. <https://doi.org/10.1002/2014TC003633>
- Law, R., Searle, M., & Simpson, R. (2004). Strain, deformation temperatures and vorticity of flow at the top of the Greater Himalayan Slab, Everest Massif, Tibet. *Journal of the Geological Society*, *161*(2), 305–320. <https://doi.org/10.1144/0016-764903-047>
- Lechmann, S. M., Schmalholz, S. M., Hetényi, G., May, D. A., & Kaus, B. J. P. (2014). Quantifying the impact of mechanical layering and underthrusting on the dynamics of the modern India-Asia collisional system with 3-D numerical models. *Journal of Geophysical Research: Solid Earth*, *119*(1), 616–644. <https://doi.org/10.1002/2012JB009748>
- Leloup, P. H., Ricard, Y., Battaglia, J., & Lacassin, R. (1999). Shear heating in continental strike-slip shear zones: model and field examples. *Geophysical Journal International*, *136*(1), 19–40. <https://doi.org/10.1046/j.1365-246X.1999.00683.x>
- Li, C., van der Hilst, R. D., Engdahl, E. R., & Burdick, S. (2008). A new global model for P wave speed variations in Earth's mantle. *Geochemistry, Geophysics, Geosystems*, *9*(5), Q05018. <https://doi.org/10.1029/2007GC001806>
- Li, C., van der Hilst, R. D., Meltzer, A. S., & Engdahl, E. R. (2008). Subduction of the Indian lithosphere beneath the Tibetan Plateau and Burma. *Earth and Planetary Science Letters*, *274*(1–2), 157–168. <https://doi.org/10.1016/j.epsl.2008.07.016>
- Li, J., Yao, Y., Li, R., Yusan, S., Li, G., Freymueller, J. T., & Wang, Q. (2022). Present-day strike-slip faulting and thrusting of the Kepingtage fold-and-thrust belt in southern Tianshan: Constraints from GPS observations. *Geophysical Research Letters*, *49*(11), e2022GL099105. <https://doi.org/10.1029/2022GL099105>
- Li, W., Chen, Y., Yuan, X., Xiao, W., & Windley, B. F. (2022). Intracontinental deformation of the Tianshan Orogen in response to India-Asia collision. *Nature Communications*, *13*(1), 3738. <https://doi.org/10.1038/s41467-022-30795-6>
- Li, Y., Liu, M., Li, Y., & Chen, L. (2019). Active crustal deformation in southeastern Tibetan Plateau: The kinematics and dynamics. *Earth and Planetary Science Letters*, *523*, 115708. <https://doi.org/10.1016/j.epsl.2019.07.010>
- Li, Y., Liu, M., Wang, Q., & Cui, D. (2018). Present-day crustal deformation and strain transfer in northeastern Tibetan Plateau. *Earth and Planetary Science Letters*, *487*, 179–189. <https://doi.org/10.1016/j.epsl.2018.01.024>
- Li, Y., Shan, X., Qu, C., Zhang, Y., Song, X., Jiang, Y., et al. (2017). Elastic block and strain modeling of GPS data around the Haiyuan-Liupanshan fault, northeastern Tibetan Plateau. *Journal of Asian Earth Sciences*, *150*, 87–97. <https://doi.org/10.1016/j.jseae.2017.10.010>
- Li, Y., Wu, Q., Pan, J., Zhang, F., & Yu, D. (2013). An upper-mantle S-wave velocity model for East Asia from Rayleigh wave tomography. *Earth and Planetary Science Letters*, *377*, 367–377. <https://doi.org/10.1016/j.epsl.2013.06.033>
- Liu, C., Ji, L., Zhu, L., Xu, C., Zhao, C., Lu, Z., & Wang, Q. (2024). Kilometer-resolution three-dimensional crustal deformation of Tibetan Plateau from InSAR and GNSS. *Science China Earth Sciences*, *67*(6), 1818–1835. <https://doi.org/10.1007/s11430-023-1289-4>

- Liu, M., & Yang, Y. (2003). Extensional collapse of the Tibetan Plateau: Results of three-dimensional finite element modeling. *Journal of Geophysical Research*, *108*(B8), 2361. <https://doi.org/10.1029/2002JB002248>
- Loveless, J. P., & Meade, B. J. (2011). Partitioning of localized and diffuse deformation in the Tibetan Plateau from joint inversions of geologic and geodetic observations. *Earth and Planetary Science Letters*, *303*(1), 11–24. <https://doi.org/10.1016/j.epsl.2010.12.014>
- Mahesh, P., Catherine, J. K., Gahalaut, V. K., Kundu, B., Ambikapathy, A., Bansal, A., et al. (2012). Rigid Indian plate: Constraints from GPS measurements. *Gondwana Research*, *22*(3), 1068–1072. <https://doi.org/10.1016/j.gr.2012.01.011>
- Mallick, R., Lindsey, E. O., Feng, L., Hubbard, J., Banerjee, P., & Hill, E. M. (2019). Active convergence of the India-Burma-Sunda plates revealed by a new continuous GPS network. *Journal of Geophysical Research: Solid Earth*, *124*(3), 3155–3171. <https://doi.org/10.1029/2018JB016480>
- Marechal, A., Mazzotti, S., Cattin, R., Cazes, G., Vernant, P., Drukpa, D., et al. (2016). Evidence of interseismic coupling variations along the Bhutan Himalayan arc from new GPS data. *Geophysical Research Letters*, *43*(24), 12–399. <https://doi.org/10.1002/2016GL071163>
- Marone, C. (1998). Laboratory-derived friction laws and their application to seismic faulting. *Annual Review of Earth and Planetary Sciences*, *26*(1), 643–696. <https://doi.org/10.1146/annurev.earth.26.1.643>
- McCaffrey, R., Long, M. D., Goldfinger, C., Zwick, P. C., Nabelek, J. L., Johnson, C. K., & Smith, C. (2000). Rotation and plate locking at the southern Cascadia subduction zone. *Geophysical Research Letters*, *27*(19), 3117–3120. <https://doi.org/10.1029/2000GL011768>
- McClusky, S. C., Bjornstad, S. C., Hager, B. H., King, R. W., Meade, B. J., Miller, M. M., et al. (2001). Present day kinematics of the Eastern California Shear Zone from a geodetically constrained block model. *Geophysical Research Letters*, *28*(17), 3369–3372. <https://doi.org/10.1029/2001GL013091>
- McKenzie, D. (1972). Active tectonics of the Mediterranean region. *Geophysical Journal International*, *30*(2), 109–185. <https://doi.org/10.1111/j.1365-246X.1972.tb02351.x>
- McNamara, D. E., Owens, T. J., Silver, P. G., & Wu, F. T. (1994). Shear wave anisotropy beneath the Tibetan Plateau. *Journal of Geophysical Research*, *99*(B7), 13655–13665. <https://doi.org/10.1029/93JB03406>
- Meade, B. J., & Hager, B. H. (2005). Block models of crustal motion in southern California constrained by GPS measurements. *Journal of Geophysical Research*, *110*(B3), B03403. <https://doi.org/10.1029/2004JB003209>
- Metzger, S., Gagala, u., Ratschbacher, L., Lazecký, M., Maghsoudi, Y., & Schurr, B. (2021). Tajik depression and greater Pamir neotectonics from InSAR rate maps. *Journal of Geophysical Research: Solid Earth*, *126*(12), e2021JB022775. <https://doi.org/10.1029/2021JB022775>
- Metzger, S., Ischuk, A., Deng, Z., Ratschbacher, L., Perry, M., Kufner, S.-K., et al. (2020). Dense GNSS profiles across the northwestern tip of the India-Asia collision zone: Triggered slip and westward flow of the Peter the First Range, Pamir, into the Tajik depression. *Tectonics*, *39*(2), e2019TC005797. <https://doi.org/10.1029/2019TC005797>
- Molnar, P., & Dayem, K. E. (2010). Major intracontinental strike-slip faults and contrasts in lithospheric strength. *Geosphere*, *6*(4), 444–467. <https://doi.org/10.1130/GES00519.1>
- Molnar, P., & Deng, Q. (1984). Faulting associated with large earthquakes and the average rate of deformation in central and eastern Asia. *Journal of Geophysical Research*, *89*(B7), 6203–6227. <https://doi.org/10.1029/JB089iB07p06203>
- Molnar, P., & Tapponnier, P. (1975). Cenozoic tectonics of Asia: Effects of a continental collision. *Science*, *189*(4201), 419–426. <https://doi.org/10.1126/science.189.4201.419>
- Molnar, P., & Tapponnier, P. (1978). Active tectonics of Tibet. *Journal of Geophysical Research*, *83*(B11), 5361–5375. <https://doi.org/10.1029/JB083iB11p05361>
- Molnar, P., & Tapponnier, P. (1981). A possible dependence of tectonic strength on the age of the crust in Asia. *Earth and Planetary Science Letters*, *52*(1), 107–114. [https://doi.org/10.1016/0012-821X\(81\)90213-2](https://doi.org/10.1016/0012-821X(81)90213-2)
- Neil, E. A., & Houseman, G. A. (1997). Geodynamics of the Tarim Basin and the Tian Shan in central Asia. *Tectonics*, *16*(4), 571–584. <https://doi.org/10.1029/97TC01413>
- Nie, S., Tian, X., Liang, X., & Wan, B. (2023). Less-well-developed crustal channel-flow in the central Tibetan Plateau revealed by receiver function and surface wave joint inversion. *Journal of Geophysical Research: Solid Earth*, *128*(4), e2022JB025747. <https://doi.org/10.1029/2022JB025747>
- Ou, Q., Daout, S., Weiss, J. R., Shen, L., Lazecký, M., Wright, T. J., & Parsons, B. E. (2022). Large-scale interseismic strain mapping of the NE Tibetan Plateau from Sentinel-1 interferometry. *Journal of Geophysical Research: Solid Earth*, *127*(6), e2022JB024176. <https://doi.org/10.1029/2022JB024176>
- Pan, Y., Chen, R., Yi, S., Wang, W., Ding, H., Shen, W., & Chen, L. (2019). Contemporary mountain-building of the Tianshan and its relevance to geodynamics constrained by integrating GPS and GRACE measurements. *Journal of Geophysical Research: Solid Earth*, *124*(11), 12171–12188. <https://doi.org/10.1029/2019JB017566>
- Pan, Y., & Shen, W.-B. (2017). Contemporary crustal movement of southeastern Tibet: Constraints from dense GPS measurements. *Scientific Reports*, *7*(1), 45348. <https://doi.org/10.1038/srep45348>
- Pan, Y., Shen, W.-B., Shum, C., & Chen, R. (2018). Spatially varying surface seasonal oscillations and 3-D crustal deformation of the Tibetan Plateau derived from GPS and GRACE data. *Earth and Planetary Science Letters*, *502*, 12–22. <https://doi.org/10.1016/j.epsl.2018.08.037>
- Pan, Z., Yun, Z., & Shao, Z. (2020). Contemporary crustal deformation of Northeast Tibet from geodetic investigations and a comparison between the seismic and geodetic moment release rates. *Physics of the Earth and Planetary Interiors*, *304*, 106489. <https://doi.org/10.1016/j.pepi.2020.106489>
- Penney, C., & Copley, A. (2021). Lateral variations in lower crustal strength control the temporal evolution of mountain ranges: Examples from south-east Tibet. *Geochemistry, Geophysics, Geosystems*, *22*(2), e2020GC009092. <https://doi.org/10.1029/2020GC009092>
- Perry, M., Kakar, N., Ischuk, A., Metzger, S., Bendick, R., Molnar, P., & Mohadjer, S. (2019). Little geodetic evidence for localized Indian subduction in the Pamir-Hindu Kush of Central Asia. *Geophysical Research Letters*, *46*(1), 109–118. <https://doi.org/10.1029/2018GL080065>
- Pullen, A., & Kapp, P. (2014). Mesozoic tectonic history and lithospheric structure of the Qiangtang terrane: Insights from the Qiangtang metamorphic belt, central Tibet. *Geological Society of America Special Papers*, *507*, 71–87. [https://doi.org/10.1130/2014.2507\(04\)114.1](https://doi.org/10.1130/2014.2507(04)114.1)
- Rey, P. F., Teyssier, C., & Whitney, D. L. (2010). Limit of channel flow in orogenic plateaux. *Lithosphere*, *2*(5), 328–332. <https://doi.org/10.1130/L114.1>
- Rollins, C. (2023). earjcr1/AHB\_GPS: V0.1 (v0.1) [Dataset]. *Zenodo*. <https://doi.org/10.5281/zenodo.10372924>
- Royden, L. H., Burchfiel, B. C., King, R. W., Wang, E., Chen, Z., Shen, F., & Liu, Y. (1997). Surface deformation and lower crustal flow in eastern Tibet. *Science*, *276*(5313), 788–790. <https://doi.org/10.1126/science.276.5313.788>
- Royden, L. H., Burchfiel, B. C., & van der Hilst, R. D. (2008). The geological evolution of the Tibetan Plateau. *Science*, *321*(5892), 1054–1058. <https://doi.org/10.1126/science.1155371>
- Rui, X., & Stamps, D. S. (2016). Present-day kinematics of the eastern Tibetan Plateau and Sichuan Basin: Implications for lower crustal rheology. *Journal of Geophysical Research: Solid Earth*, *121*(5), 3846–3866. <https://doi.org/10.1002/2016JB012839>

- Rui, X., & Stamps, D. S. (2019). A geodetic strain rate and tectonic velocity model for China. *Geochemistry, Geophysics, Geosystems*, 20(3), 1280–1297. <https://doi.org/10.1029/2018GC007806>
- Rybacki, E., Gottschalk, M., Wirth, R., & Dresen, G. (2006). Influence of water fugacity and activation volume on the flow properties of fine-grained anorthite aggregates. *Journal of Geophysical Research*, 111(B3), B03203. <https://doi.org/10.1029/2005JB003663>
- Schmalholz, S. M., Duretz, T., Hetényi, G., & Medvedev, S. (2018). Distribution and magnitude of stress due to lateral variation of gravitational potential energy between Indian lowland and Tibetan plateau. *Geophysical Journal International*, 216(2), 1313–1333. <https://doi.org/10.1093/gji/ggy463>
- Schmalholz, S. M., & Fletcher, R. C. (2011). The exponential flow law applied to necking and folding of a ductile layer. *Geophysical Journal International*, 184(1), 83–89. <https://doi.org/10.1111/j.1365-246X.2010.04846.x>
- Scholz, C. H. (1998). Earthquakes and friction laws. *Nature*, 391(6662), 37–42. <https://doi.org/10.1038/34097>
- Scholz, C. H., & Choi, E. (2022). What comes first: The fault or the ductile shear zone? *Earth and Planetary Science Letters*, 577, 117273. <https://doi.org/10.1016/j.epsl.2021.117273>
- Searle, M., Elliott, J., Phillips, R., & Chung, S.-L. (2011). Crustal–lithospheric structure and continental extrusion of Tibet. *Journal of the Geological Society*, 168(3), 633–672. <https://doi.org/10.1144/0016-76492010-139>
- Searle, M., Law, R., & Jessup, M. (2006). Crustal structure, restoration and evolution of the Greater Himalaya in Nepal–South Tibet: Implications for channel flow and ductile extrusion of the middle crust. *Geological Society, London, Special Publications*, 268(1), 355–378. <https://doi.org/10.1144/GSL.SP.2006.268.01.17>
- Searle, M., Simpson, R., Law, R., Parrish, R., & Waters, D. (2003). The structural geometry, metamorphic and magmatic evolution of the Everest massif, High Himalaya of Nepal–South Tibet. *Journal of the Geological Society*, 160(3), 345–366. <https://doi.org/10.1144/0016-764902-126>
- Searle, M., & Szulc, A. G. (2005). Channel flow and ductile extrusion of the high Himalayan slab—the Kangchenjunga–Darjeeling profile, Sikkim Himalaya. *Journal of Asian Earth Sciences*, 25(1), 173–185. <https://doi.org/10.1016/j.jseaes.2004.03.004>
- Sharma, Y., Pasari, S., Ching, K.-E., Dikshit, O., Kato, T., Malik, J. N., et al. (2020). Spatial distribution of earthquake potential along the Himalayan arc. *Tectonophysics*, 791, 228556. <https://doi.org/10.1016/j.tecto.2020.228556>
- Shen, F., Royden, L. H., & Burchfiel, B. C. (2001). Large-scale crustal deformation of the Tibetan Plateau. *Journal of Geophysical Research*, 106(B4), 6793–6816. <https://doi.org/10.1029/2000JB900389>
- Shen, Z., Lü, J., Wang, M., & Bürgmann, R. (2005). Contemporary crustal deformation around the southeast borderland of the Tibetan Plateau. *Journal of Geophysical Research*, 110(B11), B11409. <https://doi.org/10.1029/2004JB003421>
- Shen, Z.-K., Wang, M., Li, Y., Jackson, D. D., Yin, A., Dong, D., & Fang, P. (2001). Crustal deformation along the Altyn Tagh fault system, western China, from GPS. *Journal of Geophysical Research*, 106(B12), 30607–30621. <https://doi.org/10.1029/2001JB000349>
- Shewchuk, J. R. (2002). Delaunay refinement algorithms for triangular mesh generation. *Computational Geometry*, 22(1–3), 21–74. [https://doi.org/10.1016/S0925-7721\(01\)00047-5](https://doi.org/10.1016/S0925-7721(01)00047-5)
- Shi, D., Zhao, W., Brown, L., Nelson, D., Zhao, X., Kind, R., et al. (2004). Detection of southward intracontinental subduction of Tibetan lithosphere along the Bangong–Nujiang suture by P-to-S converted waves. *Geology*, 32(3), 209–212. <https://doi.org/10.1130/G19814.1>
- Shi, Y., & Cao, J. (2008). Lithosphere effective viscosity of continental China. *Earth Science Frontiers*, 15(3), 82–95. [https://doi.org/10.1016/S1872-5791\(08\)60064-0](https://doi.org/10.1016/S1872-5791(08)60064-0)
- Silver, P. G. (1996). Seismic anisotropy beneath the continents: Probing the depths of geology. *Annual Review of Earth and Planetary Sciences*, 24(1), 385–432. <https://doi.org/10.1146/annurev.earth.24.1.385>
- Singh, A., Singh, C., & Kennett, B. (2015). A review of crust and upper mantle structure beneath the Indian subcontinent. *Tectonophysics*, 644, 1–21. <https://doi.org/10.1016/j.tecto.2015.01.007>
- Socquet, A., Simons, W., Vigny, C., McCaffrey, R., Subarya, C., Sarsito, D., et al. (2006). Microblock rotations and fault coupling in SE Asia triple junction (Sulawesi, Indonesia) from GPS and earthquake slip vector data. *Journal of Geophysical Research*, 111(B8), B08409. <https://doi.org/10.1029/2005JB003963>
- Sol, S., Meltzer, A., Burgmann, R., Van der Hilst, R., King, R., Chen, Z., et al. (2007). Geodynamics of the southeastern Tibetan Plateau from seismic anisotropy and geodesy. *Geology*, 35(6), 563–566. <https://doi.org/10.1130/G23408A.1>
- Sonder, L. J., & England, P. (1986). Vertical averages of rheology of the continental lithosphere: Relation to thin sheet parameters. *Earth and Planetary Science Letters*, 77(1), 81–90. [https://doi.org/10.1016/0012-821X\(86\)90134-2](https://doi.org/10.1016/0012-821X(86)90134-2)
- Steckler, M. S., Akhter, S. H., & Seeber, L. (2008). Collision of the Ganges–Brahmaputra Delta with the Burma Arc: Implications for earthquake hazard. *Earth and Planetary Science Letters*, 273(3), 367–378. <https://doi.org/10.1016/j.epsl.2008.07.009>
- Steckler, M. S., Mondal, D. R., Akhter, S. H., Seeber, L., Feng, L., Gale, J., et al. (2016). Locked and loading megathrust linked to active subduction beneath the Indo-Burman Ranges. *Nature Geoscience*, 9(8), 615–618. <https://doi.org/10.1038/ngeo2760>
- Stenvall, C. A., Fagereng, k., & Diener, J. F. A. (2019). Weaker than weakest: On the strength of shear zones. *Geophysical Research Letters*, 46(13), 7404–7413. <https://doi.org/10.1029/2019GL083388>
- Styron, R. (2022). Contemporary slip rates of all active faults in the Indo-Asian collision zone [Preprint]. *ESSOAr*. <https://doi.org/10.1002/essoar.10512747.1>
- Styron, R., & Pagani, M. (2020). The GEM global active faults database. *Earthquake Spectra*, 36(1\_suppl), 160–180. <https://doi.org/10.1177/875529320944182>
- Su, X., Yao, L., Wu, W., Meng, G., Su, L., Xiong, R., & Hong, S. (2018). Crustal deformation on the northeastern margin of the Tibetan Plateau from continuous GPS observations. *Remote Sensing*, 11(1), 34. <https://doi.org/10.3390/rs11010034>
- Sun, Y.-J., Dong, S.-W., Fan, T.-Y., Zhang, H., & Shi, Y.-L. (2013). 3D rheological structure of the continental lithosphere beneath China and adjacent regions. *Chinese Journal of Geophysics*, 56(5), 546–558. <https://doi.org/10.1002/cjg2.20052>
- Tapponnier, P., & Molnar, P. (1976). Slip-line field theory and large-scale continental tectonics. *Nature*, 264(5584), 319–324. <https://doi.org/10.1038/264319a0>
- Tapponnier, P., & Molnar, P. (1979). Active faulting and cenozoic tectonics of the Tien Shan, Mongolia, and Baykal Regions. *Journal of Geophysical Research*, 84(B7), 3425–3459. <https://doi.org/10.1029/JB084iB07p03425>
- Thatcher, W. (2007). Microplate model for the present-day deformation of Tibet. *Journal of Geophysical Research*, 112(B1), B01401. <https://doi.org/10.1029/2005JB004244>
- Thatcher, W. (2009). How the continents deform: The evidence from tectonic geodesy. *Annual Review of Earth and Planetary Sciences*, 37(1), 237–262. <https://doi.org/10.1146/annurev.earth.031208.100035>
- Thybo, H., Perchuc, E., & Zhou, S. (2000). Intraplate earthquakes and a seismically defined lateral transition in the upper mantle. *Geophysical Research Letters*, 27(23), 3953–3956. <https://doi.org/10.1029/2000GL011636>
- Vauchez, A., Tommasi, A., & Mainprice, D. (2012). Faults (shear zones) in the Earth's mantle. *Tectonophysics*, 558–559, 1–27. <https://doi.org/10.1016/j.tecto.2012.06.006>

- Vergnolle, M., Calais, E., & Dong, L. (2007). Dynamics of continental deformation in Asia. *Journal of Geophysical Research*, *112*(B11), B11403. <https://doi.org/10.1029/2006JB004807>
- Vernant, P., Bilham, R., Szeliga, W., Drupka, D., Kalita, S., Bhattacharyya, A., et al. (2014). Clockwise rotation of the Brahmaputra Valley relative to India: Tectonic convergence in the eastern Himalaya, Naga Hills, and Shillong Plateau. *Journal of Geophysical Research: Solid Earth*, *119*(8), 6558–6571. <https://doi.org/10.1002/2014JB011196>
- Wallace, L. M., McCaffrey, R., Beavan, J., & Ellis, S. (2005). Rapid microplate rotations and backarc rifting at the transition between collision and subduction. *Geology*, *33*(11), 857–860. <https://doi.org/10.1130/G21834.1>
- Wallace, L. M., Stevens, C., Silver, E., McCaffrey, R., Lortung, W., Hasiata, S., et al. (2004). GPS and seismological constraints on active tectonics and arc-continent collision in Papua New Guinea: Implications for mechanics of microplate rotations in a plate boundary zone. *Journal of Geophysical Research*, *109*(B5), B05404. <https://doi.org/10.1029/2003JB002481>
- Walters, R. J., England, P. C., & Houseman, G. A. (2017). Constraints from GPS measurements on the dynamics of the zone of convergence between Arabia and Eurasia. *Journal of Geophysical Research: Solid Earth*, *122*(2), 1470–1495. <https://doi.org/10.1002/2016JB013370>
- Wang, D., Zhao, B., Yu, J., & Tan, K. (2020). Active tectonic deformation around the Tarim Basin inferred from dense GPS measurements. *Geodesy and Geodynamics*, *11*(6), 418–425. <https://doi.org/10.1016/j.geog.2020.09.001>
- Wang, H., & Wright, T. J. (2012). Satellite geodetic imaging reveals internal deformation of western Tibet. *Geophysical Research Letters*, *39*(7), L07303. <https://doi.org/10.1029/2012GL051222>
- Wang, H., Wright, T. J., Liu-Zeng, J., & Peng, L. (2019). Strain rate distribution in south-central Tibet from two decades of InSAR and GPS. *Geophysical Research Letters*, *46*(10), 5170–5179. <https://doi.org/10.1029/2019GL081916>
- Wang, L., & Barbot, S. (2023). Three-dimensional kinematics of the India–Eurasia collision. *Communications Earth & Environment*, *4*(1), 164. <https://doi.org/10.1038/s43247-023-00815-4>
- Wang, M., & Shen, Z.-K. (2020). Present-day crustal deformation of continental China derived from GPS and its tectonic implications. *Journal of Geophysical Research: Solid Earth*, *125*(2), e2019JB018774. <https://doi.org/10.1029/2019JB018774>
- Wang, M., Shen, Z.-K., Wang, Y.-Z., Bürgmann, R., Wang, F., Zhang, P.-Z., et al. (2021). Postseismic deformation of the 2008 Wenchuan earthquake illuminates lithospheric rheological structure and dynamics of eastern Tibet. *Journal of Geophysical Research: Solid Earth*, *126*(9), e2021JB022399. <https://doi.org/10.1029/2021JB022399>
- Wang, Q., Zhang, P.-Z., Freymueller, J. T., Bilham, R., Larson, K. M., You, X., et al. (2001). Present-day crustal deformation in China constrained by global positioning system measurements. *Science*, *294*(5542), 574–577. <https://doi.org/10.1126/science.1063647>
- Wang, W., Qiao, X., & Ding, K. (2021). Present-day kinematics in southeastern Tibet inferred from GPS measurements. *Journal of Geophysical Research: Solid Earth*, *126*(1), e2020JB021305. <https://doi.org/10.1029/2020JB021305>
- Wang, W., Qiao, X., Yang, S., & Wang, D. (2017). Present-day velocity field and block kinematics of Tibetan Plateau from GPS measurements. *Geophysical Journal International*, *208*(2), 1088–1102. <https://doi.org/10.1093/gji/ggw445>
- Wang, Y., Zhang, J., Jin, Z., & Green, H. (2012). Mafic granulite rheology: Implications for a weak continental lower crust. *Earth and Planetary Science Letters*, *353*–354, 99–107. <https://doi.org/10.1016/j.epsl.2012.08.004>
- Warner, M. (1990). Basalts, water, or shear zones in the lower continental crust? *Tectonophysics*, *173*(1), 163–174. [https://doi.org/10.1016/0040-1951\(90\)90214-S](https://doi.org/10.1016/0040-1951(90)90214-S)
- Weī, W., Unsworth, M., Jones, A., Booker, J., Tan, H., Nelson, D., et al. (2001). Detection of widespread fluids in the Tibetan crust by magnetotelluric studies. *Science*, *292*(5517), 716–719. <https://doi.org/10.1126/science.1010580>
- Wessel, P., Smith, W. H. F., Scharroo, R., Luis, J., & Wobbe, F. (2013). Generic mapping tools: Improved version released. *Eos, Transactions American Geophysical Union*, *94*(45), 409–410. <https://doi.org/10.1002/2013EO450001>
- Wright, T., Elliott, J. R., Wang, H., & Ryder, I. (2013). Earthquake cycle deformation and the Moho: Implications for the rheology of continental lithosphere. *Tectonophysics*, *609*, 504–523. <https://doi.org/10.1016/j.tecto.2013.07.029>
- Wright, T., Houseman, G., Fang, J., Maghsoudi, Y., Hooper, A., Elliott, J., et al. (2023). High-resolution geodetic strain rate field reveals dynamics of the India-Eurasia collision. *Science*. <https://doi.org/10.31223/X5G95R>
- Xu, X. (2022). *China active fault database*. Active Fault Survey Data Centre at Institute of Geology, China Earthquake Administration. <https://doi.org/10.12031/activefault.china.400.2022.db>
- Yadav, R. K., Gahalaut, V. K., & Bansal, A. K. (2021). Tectonic and non-tectonic crustal deformation in Kumaun Garhwal Himalaya. *Quaternary International*, *585*, 171–182. <https://doi.org/10.1016/j.quaint.2020.10.011>
- Yadav, R. K., Gahalaut, V. K., Bansal, A. K., Sati, S., Catherine, J., Gautam, P., et al. (2019). Strong seismic coupling underneath Garhwal–Kumaun region, NW Himalaya, India. *Earth and Planetary Science Letters*, *506*, 8–14. <https://doi.org/10.1016/j.epsl.2018.10.023>
- Yang, Y., & Liu, M. (2002). Cenozoic deformation of the Tarim plate and the implications for mountain building in the Tibetan Plateau and the Tian Shan. *Tectonics*, *21*(6), 9–19–17. <https://doi.org/10.1029/2001TC001300>
- Zhang, C.-L., Zou, H.-B., Li, H.-K., & Wang, H.-Y. (2013). Tectonic framework and evolution of the Tarim Block in NW China. *Gondwana Research*, *23*(4), 1306–1315. <https://doi.org/10.1016/j.gr.2012.05.009>
- Zhang, H., Kirby, E., Li, H., Cook, K., & Zhang, P. (2020). Ten years after the Wenchuan earthquake: New insights into the geodynamics of the eastern Tibet. *Tectonics*, *39*(6), e2020TC006215. <https://doi.org/10.1029/2020TC006215>
- Zhang, P. (2013). A review on active tectonics and deep crustal processes of the Western Sichuan region, eastern margin of the Tibetan Plateau. *Tectonophysics*, *584*, 7–22. <https://doi.org/10.1016/j.tecto.2012.02.021>
- Zhang, P., & Gan, W. (2008). Combined model of rigid-block motion with continuous deformation: Patterns of present-day deformation in continental China. In B. C. Burchfiel & E. Wang (Eds.), *Investigations into the tectonics of the Tibetan Plateau* (Vol. 444). Geological Society of America. [https://doi.org/10.1130/2008.2444\(04\)](https://doi.org/10.1130/2008.2444(04))
- Zhang, Z., Yuan, X., Chen, Y., Tian, X., Kind, R., Li, X., & Teng, J. (2010). Seismic signature of the collision between the east Tibetan escape flow and the Sichuan Basin. *Earth and Planetary Science Letters*, *292*(3), 254–264. <https://doi.org/10.1016/j.epsl.2010.01.046>
- Zhao, B., Huang, Y., Zhang, C., Wang, W., Tan, K., & Du, R. (2015). Crustal deformation on the Chinese mainland during 1998–2014 based on GPS data. *Geodesy and Geodynamics*, *6*(1), 7–15. <https://doi.org/10.1016/j.geog.2014.12.006>
- Zhao, B., Zhang, C., Wang, D., Huang, Y., Tan, K., Du, R., & Liu, J. (2017). Contemporary kinematics of the Ordos block, North China and its adjacent rift systems constrained by dense GPS observations. *Journal of Asian Earth Sciences*, *135*, 257–267. <https://doi.org/10.1016/j.jseaes.2016.12.045>
- Zhao, J., Zhang, P., Yuan, X., Gan, W., Sun, J., Deng, T., et al. (2019). Clockwise rotation of the Tarim basin driven by the Indian plate impact. *Earth Sciences and Subsoil Use*, *42*(4), 425–436. <https://doi.org/10.21285/2686-9993-2019-42-4-425-436>
- Zhao, W., & Morgan, W. J. (1987). Injection of Indian crust into Tibetan lower crust: A two-dimensional finite element model study. *Tectonics*, *6*(4), 489–504. <https://doi.org/10.1029/TC006i004p00489>

- Zheng, G., Wang, H., Wright, T. J., Lou, Y., Zhang, R., Zhang, W., et al. (2017). Crustal deformation in the India-Eurasia collision zone from 25 years of GPS measurements. *Journal of Geophysical Research: Solid Earth*, 122(11), 9290–9312. <https://doi.org/10.1002/2017JB014465>
- Zhou, Y., He, J., Oimahmadov, I., Gadoev, M., Pan, Z., Wang, W., et al. (2016). Present-day crustal motion around the Pamir Plateau from GPS measurements. *Gondwana Research*, 35, 144–154. <https://doi.org/10.1016/j.gr.2016.03.011>
- Zhu, Y., Diao, F., Wang, R., Hao, M., Shao, Z., & Xiong, X. (2022). Crustal shortening and rheological behavior across the Longmen Shan fault, eastern margin of the Tibetan Plateau. *Geophysical Research Letters*, 49(11), e2022GL098814. <https://doi.org/10.1029/2022GL098814>
- Zubovich, A., Schöne, T., Metzger, S., Mosienko, O., Mukhamediev, S., Sharshabaev, A., & Zech, C. (2016). Tectonic interaction between the Pamir and Tien Shan observed by GPS. *Tectonics*, 35(2), 283–292. <https://doi.org/10.1002/2015TC004055>

## References From the Supporting Information

- Blewitt, G., Hammond, W. C., & Kreemer, C. (2018). Harnessing the GPS data explosion for interdisciplinary science. *Eos*, 99. <https://doi.org/10.1029/2018EO104623>
- Blewitt, G., & Lavallée, D. (2002). Effect of annual signals on geodetic velocity. *Journal of Geophysical Research*, 107(B7), ETG 9–1–ETG 9–11. <https://doi.org/10.1029/2001JB000570>
- Stevens, V., & Avouac, J. (2021). On the relationship between strain rate and seismicity in the India–Asia collision zone: Implications for probabilistic seismic hazard. *Geophysical Journal International*, 226(1), 220–245. <https://doi.org/10.1093/gji/ggab098>